THE ASTROPHYSICAL JOURNAL, 460:320–333, 1996 March 20

# *HUBBLE SPACE TELESCOPE* OBSERVATIONS OF PLANETARY NEBULAE IN THE MAGELLANIC CLOUDS. IV. [O III] IMAGES AND EVOLUTIONARY AGES

M. A. DOPITA,[1] E. VASSILIADIS,[2] S. J. MEATHERINGHAM,[1] R. C. BOHLIN,[2] H. C. FORD,[2]
J. P. HARRINGTON,[3] P. R. WOOD,[1] T. P. STECHER,[4] AND S. P. MARAN[4]

*Received 1995 May 9; accepted 1995 July 26*

## ABSTRACT

The Planetary Camera of the *Hubble Space Telescope* has been used to obtain images in the [O III] λ5007 line for a sample of 15 planetary nebulae in the Magellanic Clouds chosen to eliminate any selection bias in either excitation class or in flux [for log $F(\mathrm{H}\beta) > -13.7$ ergs cm$^{-2}$ s$^{-1}$]. These images are used to derive the physical dimensions, the spatial structure, and the kinematic ages of the nebulae. The raw images were deconvolved using the Richardson-Lucy image restoration algorithm, and based on extensive tests of model images, a limit of 100 iterations of the algorithm was adopted. The restored images show clear evidence for size evolution across the H-R diagram. The younger, low-excitation, compact planetary nebulae tend to be systematically smaller than photoionization models based on ground-based data would predict, suggesting that these planetary nebulae have a central reservoir of dense atomic and molecular gas. This gas lies close to the central star and is undergoing ionization and being accelerated into outflow. Planetary nebulae previously classified as nitrogen-rich objects with massive central stars (Peimbert type I) show the bipolar "butterfly" symmetry that is also a characteristic of their Galactic counterparts. The derived kinematic ages range from less than 1000 yr up to almost 5000 yr but show little sign of systematic increase along the evolutionary tracks. The true ages of the larger objects are systematically underestimated because of acceleration of the nebular shell during its lifetime. Using both the empirical fit that we had previously derived for the expansion velocity as a function of the position on the H-R diagram, and the theoretical evolutionary tracks of the central star, we have derived two semiempirical estimates for the evolutionary timescales based upon the nebular size and the measured dynamical age. If these evolutionary timescales are to be consistent with the evolutionary age derived from theory, then He burners outnumber H burners in the approximate ratio 2:1.

*Subject headings:* ISM: structure — Magellanic Clouds — planetary nebulae: general — stars: evolution

## 1. INTRODUCTION

The evolution of stars from the termination of the asymptotic giant branch (AB) evolution through the planetary nebula (PN) stage represents a fascinating stage of stellar evolution. In the case of Galactic objects, the study of this phase of evolution is beset by gross uncertainties in the PN distance scale. This results in poor observational constraints to the often complex theoretical evolutionary scenarios of PN central stars or "nuclei" (PNn) proposed in the literature (e.g., Vassiliadis & Wood 1993; Iben 1984). In particular, we would like to reconcile the apparent differences between dynamical ages derived for the PN and the evolutionary timescales implied for the central star on the basis of theory (McCarthy et al. 1990). These problems are best resolved by study of a population of stars at known distance and having low field reddening. For these purposes, the Magellanic Cloud PNs are ideal. At optical wavelengths, this population has already been the subject of a systematic and detailed observational study both by us and by the University Colledg group. Data on the line fluxes, the nebular densities, the expansion velocities, and the kinematics have all been accumulated in the last few years (see the review by Barlow 1989; also Dopita et al. 1985; Dopita, Ford, & Webster 1985; Meatheringham et al. 1988; Meatheringham, Dopita, & Morgan 1988; Wood, Bessell, & Dopita 1986; Wood et al. 1987; and Jacoby, Walker, & Ciardullo 1990).

However, a key observational parameter which is not easily accessible to ground-based observation is the size and internal morphology of the nebula. Sizes have been derived for only the largest PN having diameters >1".0 (Jacoby 1980; Wood et al. 1987; Jacoby et al. 1990; Jacoby & Kaler 1993). Although information on smaller spatial scales has been derived using speckle interferometric techniques (Wood et al. 1986), the interpretation of these data can be difficult, and often this leads to somewhat ambiguous results. However, the imaging capability of the *Hubble Space Telescope* (*HST*) allows us to both measure the size and to resolve the details of the internal structure of the Magellanic Cloud PNs. Furthermore, the spectroscopic capability of the *HST* is ideal for the study of the UV spectra of these PNs. Therefore, we have undertaken an integrated imaging and spectroscopy program using instruments aboard the *HST* to achieve a better understanding of the PNs in the Magellanic Clouds. In Papers I and II (Dopita et al. 1993, 1994) we demonstrated how fully self-consistent nebular models can be constructed using the *HST* data set in conjunction with the ground-based data. In Paper I, a Peimbert type 1 PN having a massive planetary nebula nucleus (PNn) and a filamentary optically thin nebula was studied, and in Paper II, a model for a low-excitation compact optically thick nebula was given. In this paper we report on the cycle 1 imaging results we have

---

[1] Mount Stromlo and Siding Spring Observatories, Institute of Advanced Studies, The Australian National University, Private Bag, Weston Creek P.O., ACT 2611, Australia.

[2] Space Telescope Science Institute, 3700 San Martin Drive, Baltimore, MD 21218.

[3] Department of Astronomy, The University of Maryland, College Park, MD 20742-2421.

[4] NASA Goddard Space Flight Center, Code 680, Greenbelt, MD 20771.

obtained with the Planetary Camera through the narrowband F502N filter which isolates the [O III] λ5007 emission line. The spectroscopic results for these objects is the subject of Paper III (Vassiliadis et al. 1996), and detailed photoionization modeling of these PNs will be the subject of future papers.

The *HST* images presented in this paper were obtained in the presence of the spherical aberration intrinsic to the primary mirror (Burrows et al. 1991). However, with the long exposures on these objects and the subsequent use of computer image restoration methods, the unblurred image quality has been regained to some extent. This had already been demontrated for the specific case of the PNs observed with the Faint Object Camera, where features down to 0".1 could be distinguished (Blades et al. 1992). Similar results were reported in Papers I and II using the somewhat undersampled but high–signal-to-noise ratio images of the Planetary Camera.

The Richardson-Lucy (hereafter RL) method (Richardson 1972; Lucy 1974; Snyder 1990) is one of the major algorithms used for reconstruction of *HST* images, and this is the method that has been adopted in this paper. Other methods may offer slight improvements in image quality, but only in specific cases (e.g., King et al. 1991). For example, the damping method is not required because there is no confusion between nebular and stellar sources in our images. To understand, to parameterize, and to address the shortcomings of the RL method (e.g., White 1993), here we have constructed a series of model images for the case of both an extended nebula and the case of a central stellar source embedded in an extended nebula convolved with a typical observed *HST* point-spread function. The quality of the restored image is then examined as a function of the number of iterations, to determine the parameters required for optimum reconstruction of the observed images.

## 2. OBSERVATIONS

A sample of 15 Magellanic Cloud PNs were observed through the F502N filter of the Planetary Camera (PC) of the *HST* in the period from 1991 October to 1992 November. Of the 15 objects observed, four are in the Small Magellanic Cloud (SMC) and the remaining 11 are in the Large Magellanic Cloud (LMC). These objects are identified by their Sanduleak, MacConnell, & Philip (1978) catalog numbers (i.e., LMC-SMP 8 in the LMC, or SMC-SMP 28 in the SMC). Since the objective of this program is to deter-

TABLE 1

OBSERVATION LOG

| Object | Rootname | Observed (UT) | $t_{\rm exp}$ (s) | Counts (DN) | $x$ (pixels) | $y$ (pixels) | (Re) Processed |
|---|---|---|---|---|---|---|---|
| PSF ................ | W0SK0101T | 1991 Oct 24 | 800 | 4095[a] | 276.000 | 233.000 | 1992 Aug 13 |
| | W0SK0102T | | 639 | 3477 | 276.000 | 233.000 | |
| | W0SK0103T | | 800 | 3867 | 269.336 | 256.746 | |
| SMC-SMP 1 ....... | W0SK0201T | 1992 Oct 2 | 1700 | 2663 | 293.828 | 285.086 | 1992 Oct 3 |
| | W0SK0202T | | 1700 | 2668 | 293.785 | 285.123 | |
| SMC-SMP 3 ....... | W0SK0301T | 1991 Dec 15 | 700 | 741 | 261.684 | 271.072 | 1992 Aug 19 |
| | W0SK0302T | | 541 | 681 | 261.602 | 271.130 | |
| SMC-SMP 6 ....... | W0SK0401T | 1992 Feb 10 | 400 | 1631 | 358.908 | 177.737 | 1992 Aug 20 |
| | W0SK0402T | | 400 | 1621 | 358.810 | 177.677 | |
| SMC-SMP 28 ...... | W0SK0601T | 1991 Dec 15 | 1525 | 897 | 312.325 | 272.335 | 1992 Aug 19 |
| | W0SK0602T | | 1700 | 956 | 312.400 | 272.349 | |
| | W0SK0603T | | 1700 | 965 | 312.443 | 272.368 | |
| LMC-SMP 2 ....... | W0SK0701T | 1991 Oct 24 | 1500 | 752 | 274.883 | 256.832 | 1992 Aug 13 |
| | W0SK0702T | | 1332 | 725 | 275.151 | 256.939 | |
| | W0SK0703T | | 1500 | 751 | 275.119 | 256.888 | |
| LMC-SMP 8 ....... | W0SK0801T | 1991 Oct 25 | 500 | 2065 | 178.909 | 337.049 | 1992 Aug 14 |
| | W0SK0802T | | 305 | 1389 | 179.044 | 337.126 | |
| LMC-SMP 20...... | W0SK0901T | 1991 Oct 24 | 1500 | 651 | 281.570 | 356.039 | 1992 Aug 13 |
| | W0SK0902T | | 1500 | 661 | 281.932 | 356.928 | |
| LMC-SMP 35...... | W0SK0A01T | 1992 Feb 17 | 427 | 612 | 288 | 274 | 1992 Aug 21 |
| LMC-SMP 40...... | W0SK0B01T | 1992 Sep 20 | 900 | 657 | 251 | 283 | 1992 Sep 20 |
| | W0SK0B02T | | 900 | 655 | 251 | 283 | |
| LMC-SMP 47...... | W0SK0C01T | 1991 Oct 24 | 400 | 2327 | 232.998 | 289.510 | 1992 Aug 13 |
| LMC-SMP 72...... | W0SK0D01T | 1991 Oct 24 | 1810 | 507 | 244 | 294 | 1991 Aug 14 |
| | W0SK0D02T | 1991 Oct 25 | 2000 | 511 | 244 | 294 | 1992 Aug 18 |
| LMC-SMP 76...... | W0SK0E01T | 1991 Oct 24 | 400 | 1689 | 250.907 | 319.731 | 1992 Aug 13 |
| | W0SK0E02T | | 400 | 1679 | 250.765 | 319.647 | |
| LMC-SMP 85...... | W0SK0F01T | 1991 Oct 25 | 600 | 2097 | 281.762 | 255.722 | 1992 Aug 18 |
| | W0SK0F02T | | 600 | 2073 | 281.792 | 255.665 | |
| LMC-SMP 87...... | W0SK0I01T | 1991 Oct 25 | 600 | 643 | 274.720 | 249.693 | 1992 Aug 18 |
| LMC-SMP 96...... | W0SK0J01T | 1992 Feb 13 | 600 | 549 | 94.308 | 227.838 | 1992 Aug 20 |
| | W0SK0J02T | | 466 | 529 | 93.101 | 226.524 | |

[a] Maximum limit of Planetary Camera.

mine the general characteristics of the post-AGB evolution of the central stars as a function of mass of the PNn, the sample was selected to span a wide range in the "observational" Hertzsprung-Russell diagram, which is the log H$\beta$–excitation class plane. By contrast, the guaranteed-time observer (GTO) proposals were biased toward both bright and high-excitation PNs. The objects we observed are listed in Table 1, except for SMC-SMP 7. There were two attempts to observe this object, but both failed as a result of guide star acquisition failures in crowded fields. Given the limited spacecraft resources, it is unlikely that this observation will be attempted again.

The F502N filter is centered at a wavelength of $\lambda = 5018.5$ Å and has an FWHM bandpass of 29.7 Å (see Appendix A of MacKenty et al. 1992). Although PC 6 was later found to be the optimum chip to use, these observations were made with chip PC 8 on the basis of its greater sensitivity (see Fig. 4.1 of MacKenty et al. 1992). All images were offset from the nominal chip center by approximately 14'' in the direction of the pyramid vertex in order to avoid the Baum spot. The nominal, or reference, pixel position to which the target coordinates are assigned fell at (260, 260). The scatter in the final positions as measured on PC 8 had $\sigma = 1''.64$, which we believe resulted from poor initial measurement of coordinates from the Guide Star Selection System (GSSS) and the pointing error of the telescope. With respect to the first error, we should note that the GSSS fields are digitized at the relatively poor spatial scale of $1''.67$ pixel$^{-1}$. The coordinates listed in Table 2 are those obtained by improved measurements of the GSSS data, which are expected to be accurate to within $0''.4$ relative to the Guide Star Catalogue (GSC) reference frame. The remeasured PN coordinates scatter by only $\sigma = 0''.81$ with respect to the PC 8 frame of reference.

In addition to the PN targets, a bright star near LMC-SMP 85 was observed to provide a point-spread function (PSF) at high signal-to-noise ratio suitable for deconvolution purposes. This star is in the GSC, has a magnitude of $V = 12.7 \pm 0.35$, and is located approximately 15'' northeast of LMC-SMP 85. We have designated this as PSF-STAR throughout the remainder of the paper. The full observation log is given in Table 2.

## 3. DATA REDUCTION AND DECONVOLUTION

### 3.1. *Flat Fields*

Up to 1992 February 3, the WF/PC science instrument was operated in a continuous cold mode. On this date, the first decontamination event was executed to restore nominal performance of the cameras. The procedure resulted in the reappearance of the "measles" contaminants, which are structures typically seen at the ~1% level across the whole field of view (MacKenty & Baggett 1992).

All WF/PC exposures were flat-fielded by a series of EARTH-CAL observations obtained during the First Science Verification phase of the mission. No further EARTH-CAL observations were obtained because they are very time intensive to produce. Consequently, in principle, WF/PC exposures following any decontamination event require an updated flat-field correction. This flat-field correction is achieved by multiplying the final calibrated data product from the Space Telescope Science Institute (STScI) by a "delta" flat field, which is the ratio of the Science Verification phase flat field to an internal flat field taken after the decontamination event and as close as possible to the science observation. The dates on which the PN observations were taken are listed in Table 1. Objects SMC-SMP 6 and LMC-SMP 35 and 96 were observed following the first decontamination event. Objects SMC-SMP 1 and LMC-SMP 40 were observed following the fifth decontamination event. In practice, we did not use these "delta" flats, since for deconvolution they offered no improvement, and the photometric results were degraded by their application.

The measles contamination has been reported to be stable between decontamination events. Consequently,

TABLE 2

GSSS COORDINATE LIST FOR SMP OBJECTS

| Object[a] | $\alpha$ (J2000.0) | $\delta$ (J2000.0) | $\Delta\alpha$[b] | $\Delta\delta$[c] | Other Names | Reference |
|---|---|---|---|---|---|---|
| PSF-STAR ......... | $05^{h}40^{m}34^{s}.45$ | $-66°17'23''.1$ | ... | ... | GSC 0889102421 | 1 |
| SMC-SMP 1 ....... | 00 23 58.90 | −73 38 04.1 | +0''.5 | −0''.2 | N1, Ln2 | 2, 3 |
| SMC-SMP 3 ....... | 00 34 21.90 | −73 13 20.8 | −0.6 | +0.1 | N4, Ln16 | 2, 3 |
| SMC-SMP 6 ....... | 00 41 27.76 | −73 47 05.9 | +0.5 | −2.1 | N6, Ln33 | 2, 3 |
| SMC-SMP 28 ...... | 01 24 11.84 | −74 02 32.1 | +0.7 | −2.1 | Ln536 | 3 |
| LMC-SMP 2 ....... | 04 40 56.74 | −67 48 02.7 | +0.2 | +0.5 | ... |  |
| LMC-SMP 8 ....... | 04 50 13.10 | −69 33 57.1 | −0.4 | −1.4 | N78, LM1-5 | 2, 4 |
| LMC-SMP 20...... | 05 04 40.14 | −69 21 39.3 | +1.6 | −2.4 | LM2-5 | 5 |
| LMC-SMP 35...... | 05 10 49.97 | −65 29 30.7 | −0.3 | +0.1 | WS12, LM1-22 | 4, 6 |
| LMC-SMP 40...... | 05 12 15.63 | −66 22 56.8 | −0.2 | −0.4 | WS16 | 6 |
| LMC-SMP 47...... | 05 19 54.71 | −69 31 05.3 | +0.1 | −2.0 | N122, LM1-28, WS18, J25 | 2, 4, 6, 7 |
| LMC-SMP 72...... | 05 30 45.98 | −70 50 16.4 | +0.4 | −0.6 | ... |  |
| LMC-SMP 76...... | 05 33 56.20 | −67 53 08.4 | +0.7 | −0.6 | N60, WS32 | 2, 6 |
| LMC-SMP 85...... | 05 40 30.87 | −66 17 37.3 | +0.2 | +1.0 | N69, LM1-54 | 2, 4 |
| LMC-SMP 87...... | 05 41 08.12 | −72 42 08.2 | 0.0 | +0.7 | N215, LM1-55, WS37 | 2, 4, 6 |
| LMC-SMP 96...... | 06 06 05.45 | −71 04 14.9 | −1.0 | −1.9 | ... |  |

[a] SMP = Sanduleak, MacConnell, & Philip 1978.

[b] Right ascension offset, in arcseconds, of the GSSS coordinates with respect to the reference pixel on PC 8.

[c] Declination offset, in arcseconds, of the GSSS coordinates with respect to the reference pixel on PC 8.

REFERENCES.—(1) Guide Star Catalog. (2) Henize 1956. (3) Lindsay 1961. (4) Lindsay & Mullan 1963, Table 1. (5) Lindsay & Mullan 1963, Table 2. (6) Westerlund & Smith 1964. (7) Jacoby 1980.

1996ApJ...460..320D

average delta flat fields have been produced by STScI and are available from the *HST* archive. However, the average delta flat fields were only obtained through four specific filters. Of these, only the F547M is close in wavelength to the F502N filter used in this investigation. The average delta flat field appropriate for observations after the 1992 February 4 decontamination event is identified by the code CC210484W\@. The average delta flat field appropriate for observations after the 1992 August 7 decontamination event is D410847KW\@.

Calibrated data were usually made available to us within days from the time of observation for each object. All data obtained prior to 1992 September were reprocessed through the standard data reduction pipeline by STScI to update the astrometry, flat-fielding, header keywords, etc. Data obtained after this date were processed through the standard pipeline for WF/PC data at the STSci (Lauer 1989).

### 3.2. *Choice of the PSF to be Used*

The PSF of the PC is known to be dependent on a number of variables (Burrows et al. 1991). These are primarily the spatial position in the focal plane and the wavelength and bandpass of the observations. However, there also occur drifts due to long-term desorption in the telescope and instrument structure, and short-term "breathing" varying temperature gradients set up in the structure throughout the orbit. Furthermore, there are the occasional one-off changes due to adjustments of telescope focus. Consequently, ideally one requires an observed PSF obtained at the same time as each science observation. However, this is impracticable, and as the observation log shows we essentially have only one PSF image obtained at the very beginning of the program instead of three separate measurements taken through the program, as we had originally requested. At the time this work was carried out, there were no observed PSFs in the STScI WFPC PSF Library (located within the *HST* archive) which were relevant to the F502N filter and the PC 8 chip.

Tiny-Tim is an independently maintained program available at STScI which attempts to recreate the observed PSF at any pixel position and for any camera (Krist 1992, 1994). Thus, the only valid comparison we can make is between the observed and modeled PSFs at the chip position of the observed PSF, as shown in Figure 1. The observed PSF was generated by combining exposures W0SK0101T and W0SK0102T, and version 2.1 of the Tiny-Tim software was used to generate the model PSF. Subsequent versions of Tiny-Tim offer only a marginal improvement and do not affect the discussion below.

The difference in position of the first subsidiary maximum, located at approximately 0".8 from the PSF core center, appears to indicate a difference in the telescope focus, determined by the secondary mirror position. Through trial and error, it was discovered that the outer portions of the Tiny-Tim–generated PSF can be made to match its observed counterpart if the focus of the Tiny-Tim PSF is adjusted by about +6 μm. However, a change of this much in the focus would result in a noticeable degradation in the encircled energy profile of the resultant PSF, largely as a result of loss in sharpness of the PSF core. Since this is not seen in the observed PSF, such a large change in focus seems excessive. However, recent work at STScI has indicated that orbital "breathing" can result in as much as 2–5 μm in equivalent secondary mirror motion. In addition, longer term variations of 3–15 μm from the best, or nominal, focus have been observed (Hasan, Burrows, & Schroeder 1993).

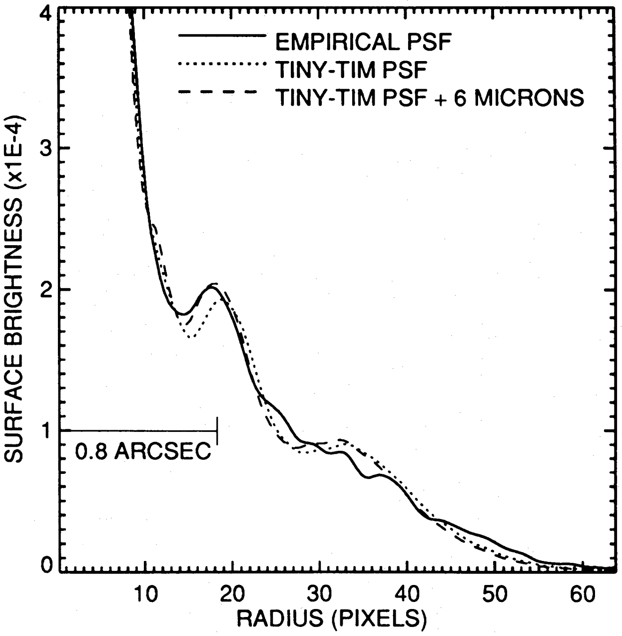

FIG. 1.—The radial distribution of the surface brightness in the PSF as determined by direct measurement of a star near LMC-SMP 85 (empirical PSF) compared with that predicted by the Tiny-Tim model, and by the Tiny-Tim model including an additional focus error of +6 μm.

One should also note from Figure 1 that the subsidiary minima and maxima of the observed PSF profile are much less distinct than in the modeled version. This effect has also been seen in other PC data (e.g., Baxter et al. 1993), and this appears to be a limitation of the Tiny-Tim software, perhaps attributable to inadequate treatment of microroughness, scattering, and guiding jitter. At the time the observed PSF was recorded, jitter was known to have a magnitude up to 30 mas. In our Tiny-Tim PSF, we assumed an average value of 15 mas. In practice, the PN images essentially show broad, slowly varing features which are well reconstructed through deconvolution with either choice of PSF. The essential difference between the PSFs is seen at the highest spatial frequencies, which the Tiny-Tim PSF will tend to amplify more rapidly in the process of image deconvolution. Given the known limitations of the Tiny-Tim PSF in accounting for microroughness, scattering, and guiding jitter, we have elected to use our observed PSF in the deconvolution process throughout the remainder of this paper.

### 3.3. *Preparation of Images for Deconvolution*

In order to generate a reliable deconvolution, it is very important to remove any artifacts in the PSF or in the science targets. In particular, bad pixels and cosmic-ray hits must be cleaned from the images before processing. For nearly all objects, multiple exposures were obtained to ensure the detection of cosmic rays. In these instances, the Image Reduction Analysis Facility (IRAF) task *stsdas.combine* was employed to combine frames, using the *crreject* option. This averaged together the frames, and the cosmic rays were flagged and removed.

In three instances in which the object was expected to have a particularly large surface brightness, only a single exposure was obtained. In these cases, cosmic-ray contamination of the image was expected to be low. Consequently, a software-based iterative technique was used to remove the cosmic rays. This used version 1.42 of the IMGCLEAN software, written by E. Deutsch and implemented within the Interactive Data Language (IDL). This proved to be adequate for the purpose, but particular attention needed to be directed to the brighter central regions of images, where the chances of missing a cosmic-ray event by visual inspection are highest. Finally, any features such as hot pixels, or remnants of cosmic-ray events which remained in the image frames, were removed manually by replacing these deviant pixel values with the median value derived from their local neighbors.

Nonlinear deconvolution techniques require that the background be positive, or as close to zero as possible. To accommodate both the low and high spatial frequencies, we have adopted the Baade-Lucy method (Baade & Lucy 1989) to set the background levels in our images and in the PSF. Lindler has developed an IDL code based on this method, and this is used here. A zero background ensures that no spurious "holes" can be dug out of the image as a result of the deconvolution process.

In other efforts to minimize the effects of noise in the deconvolution through the addition of noise in the measured PSF, the smallest possible region was extracted from the observational frames; a circular region 128 pixels in diameter, which corresponds to a PSF radius of $\sim 3''$.

### 3.4. *Tests of the Deconvolution Procedure*

Given the tendency to produce image artifacts which is inherent in the deconvolution procedure on noisy data, we must first undertake a number of tests with model images in order to determine the appropriate number of iterations of the RL method, to understand the image properties and the photometric reliability, and, in particular, to discover what artifacts might result from its use.

These model images were constructed using the IRAF task *noao.artdata.mkobjects*. Each synthetic image consists of a central star and a uniform disk simulating a nebula of radius $1\rlap{.}''0$ ($\sim 23$ Planetary camera [PC] pixels). In all cases the brightness of the disk was set to 20 counts pixel$^{-1}$, and the brightness of the central star was varied. These star plus disk profiles were convolved with the observed *HST* PSF described earlier, and the result was added to a 128 × 128 pixel sample of sky extracted from the combined PSF frames. This ensured that the synthetic data had noise characteristics similar to real data obtained with the PC 8 chip.

Models for the "ideal" restorations are constructed by convolving the model image without noise or effects of the *HST* PSF, with a two-dimensional Gaussian PSF having a full width at half-maximum of $0\rlap{.}''1$ ($\sim 2.3$ PC pixels). A sample of the images is shown in Figure 2. We considered nine values of the ratio, $R$, of the total flux from the central star to the that of the disk: 0.02, 0.05, 0.1, 0.2, 1, 5, 10, 20, and 50. Restored images were recorded after 70, 100, 250, 500, and 1000 iterations of the RL algorithm.

The IRAF task *noao.digiphot.apphot.qphot* was used to measure the counts in each restored image. The aperture was given a radius of 12 pixels, sufficiently large to encircle the stellar core, but including also portions of the reconstructed image of the nebular disk. The outer radius of the sky annulus was chosen to coincide with the edge of the nebular disk (at a radius of 23 pixels). Hence, the sky value returned by *qphot* was the mean surface brightness of the restored disk. This measurement has been used to construct Figure 3. Having subtracted the underlying sky background, *qphot* also returns the flux attributable to the central source within the aperture 12 pixels in radiux. This measurement was used to construct Figure 4. Both quantities are normalized to the corresponding measurements made on the "ideal" model images.

Figure 3 shows the normalized surface brightness of the disk with respect to $R$ as a function of the number of RL iterations on the "observed" model images (i.e., including the effect of the telescope PSF and the CCD noise). The surface brightness of the reconstructed disk begins to deviate significantly from the correct value after 100 iterations of the RL algorithm when $R \lesssim 1$. For $R \gtrsim 1$, divergence becomes apparent after only 70 iterations.

The behavior of the normalized flux derived for the central source as a function of the number of RL iterations is shown in Figure 4. The sharp rise seen at low values of $R$, which becomes more pronounced for a higher number of RL iterations, is caused by a spurious redistribution of flux from the disk into the central source. The perimeter of the disk remains well defined and observable, but the accuracy of any surface brightness determination of the disk declines as a result of noise amplification. For large values of $R$, even the structure of the underlying disk is destroyed, and after a certain number of iterations, depending on the value of $R$, all the flux is subsumed into the reconstructed image of the central source.

For models in which the central star is dominant, 100 iterations are still insufficient to restore the central star to a point source. In this case, the nebular disk remains confused with residuals from the star. Increasing the number of iterations had two effects. First, the bright central star is closer to being fully restored. Second, any attempt to determine the nebular surface brightness suffers because of noise amplification and ringing effects. This experiment clearly demonstrates the limitations of dynamic range in the RL method. The rates of convergence exhibited by the RL method will be dependent on both the brightness of the object being reconstructed, and upon the brightness and complexity of the region of sky surrounding it. Thus, while 100 RL iterations appear to be appropriate in this case, they may be an inadequate compromise in other situations. Further details on the RL method can be found in White (1993).

Two further tests are performed to examine the effect of the RL method. In the first, 10 images are created, each having a disk of uniform surface brightness, and with the radius increasing from two to 10 pixels, in steps of one pixel. These simulated data are convolved with the observed *HST* PSF. In contrast to the simulated data generated above, the disk surface brightness of the disk used here is fixed at $>2000$ counts pixel$^{-1}$, so that any effects of CCD and shot noise are unimportant. The resultant images are subjected to 100 RL iterations, and the resultant surface brightness profiles are shown in Figure 5. After the true edge of each disk is reached, the surface brightness once again appears to fall off as $R^{-4}$, the same as a reconstructed PSF. While this demonstrates the limitations in the dynamic range of the RL method, it also provides us with a means whereby we can recognize the true edge of an extended image.

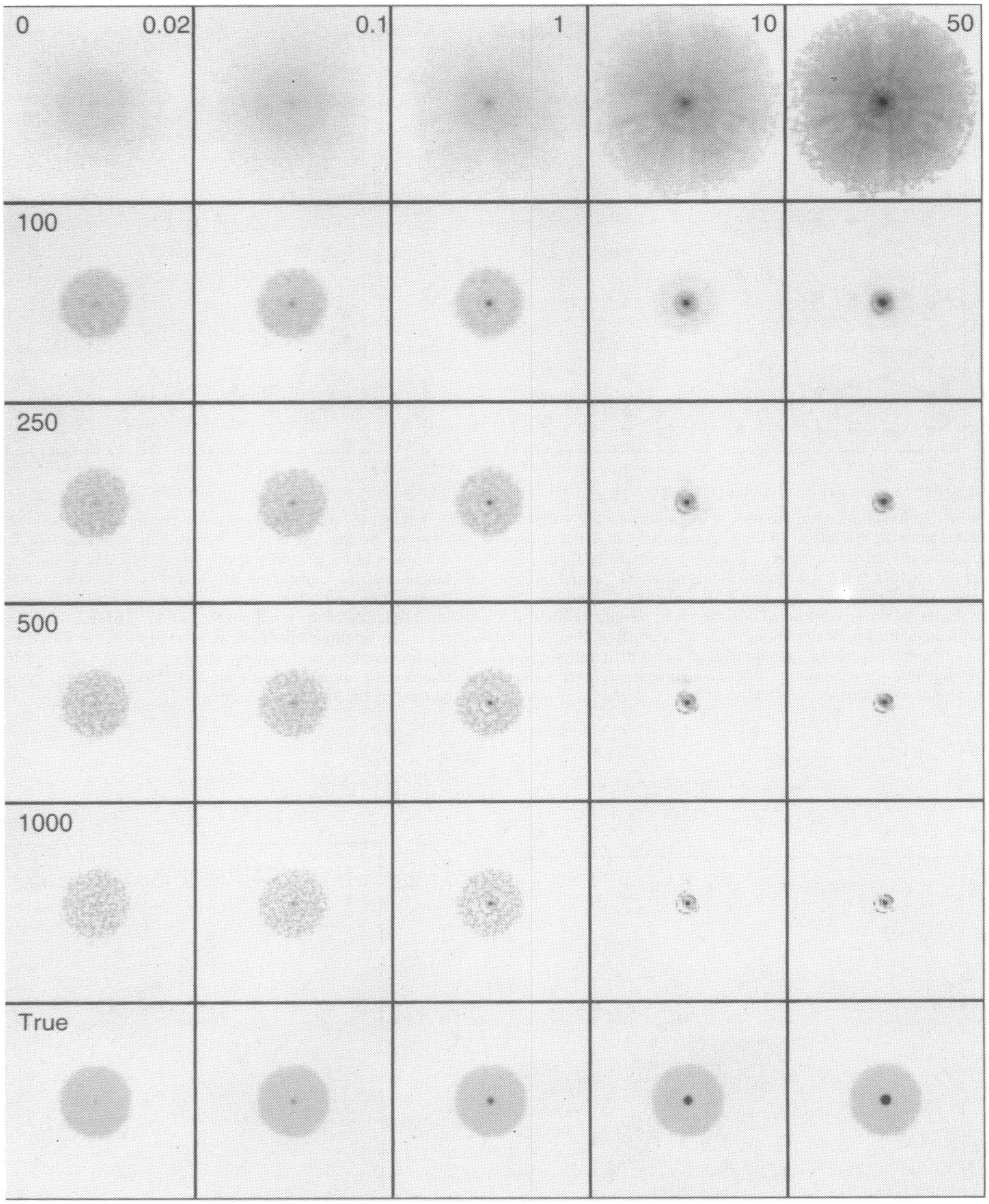

FIG. 2.—Tests of the RL deconvolution procedure on synthetic PN images consisting of a central star in a uniform extended disk of light (nebula) convolved with the observed PSF, and with CCD noise added. The ratio of the total flux from the central star to that of the disk increases from left to right and is set at 0.02, 0.1, 1, 10, and 50 in each column. The " true " image is shown in the last row, and the restored images are shown in successive rows after 100, 250, 500, and 1000 iterations of the RL algorithm. Clearly, 100 iterations represents the best compromise between resolution, photometric veracity, and freedom from artifacts.

For the second test, a central point source is added to each of the 10 disk images prior to convolution with the observed *HST* PSF. The total counts from the central source are constrained to be equal to the total counts in the disk. Figure 6 shows the resultant surface brightness profiles after 100 RL iterations. Comparing these results with those in Figure 5, it can be seen that the central point source has little effect on the falloff of apparent surface brightness beyond the true edge of the disk. Therefore, we may conclude that the appearance of a slope in the apparent surface brightness of $\sim R^{-4}$ signifies the position of the true edge of the nebular disk.

1996ApJ...460..320D

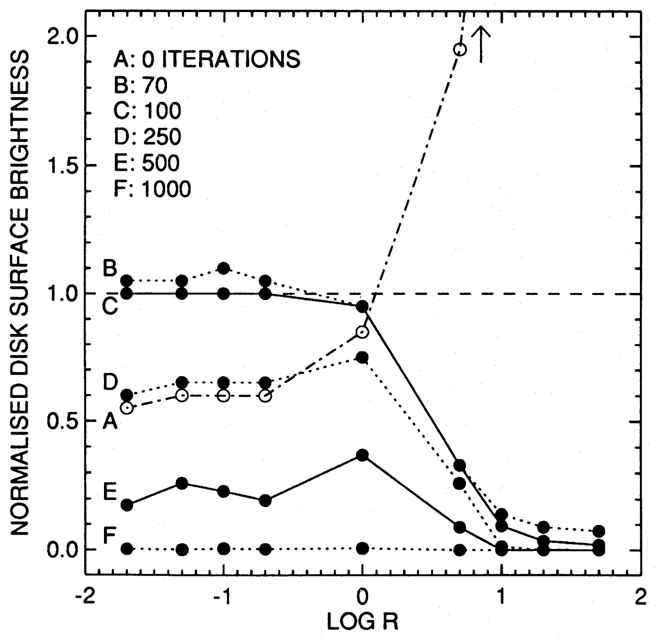

FIG. 3.—A photometric test of the surface brightness of the "nebular" disk measured from the test images of Fig. 2 as a function of *R*, the ratio of brightness of the central star compared with that of the nebula, and as a function of the number of RL iterations on the "observed" model images (i.e., including the effect of the telescope PSF and the CCD noise). The surface brightness of the reconstructed disk begins to deviate significantly from the correct value after 100 iterations of the RL algorithm when $R \lesssim 1$. For $R \gtrsim 1$, divergence becomes apparent after only 70 iterations. For values of *R* significantly greater than unity, the surface brightness of the nebula can never be restored by the RL algorithm.

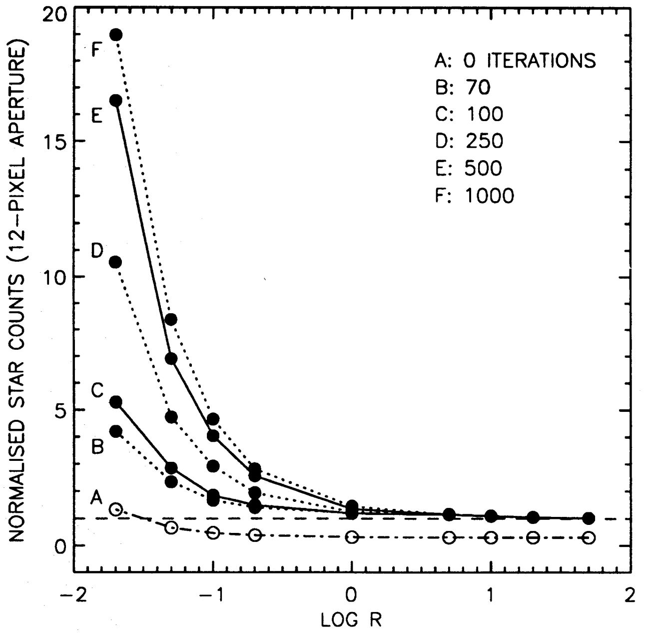

FIG. 4.—A photometric test of the brightness of the central star returned by the test images of Fig. 2 as a function of *R*, the ratio of brightness of the central star compared with that of the nebula, and as a function of the number of RL iterations. For values of *R* significantly greater than unity, the correct brightness of the central star is returned, independently of the number of iterations. However, for low values of *R*, the stellar brightness is significantly overestimated. This effect is worse for greater numbers of iterations, showing that the effect of too many iterations is to absorb the nebular flux into that of the central star while conserving the total flux in the image.

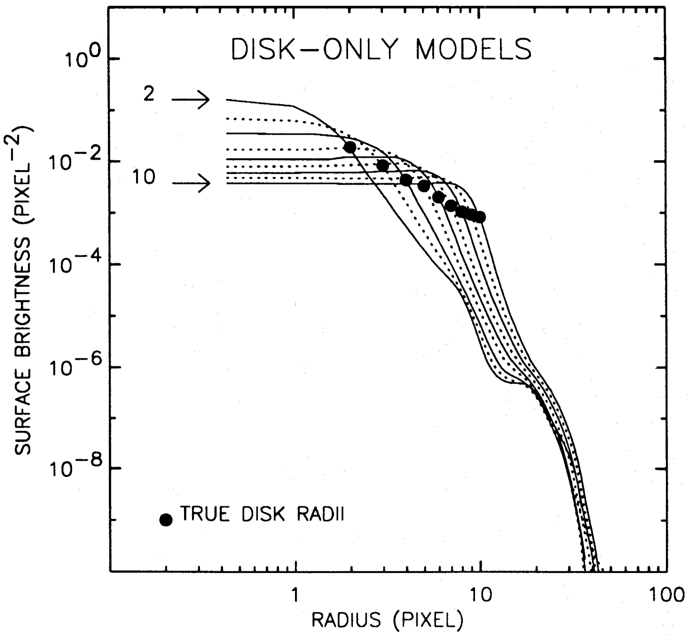

FIG. 5.—Reconstructed images of uniform, noise-free model nebular disks after 100 iterations of the RL algorithm. The radii of the disks increase from 2 PC pixels to 10 PC pixels in steps of one. Note that the true disk surface brightness is restored in the core of each disk, and that the true edge of the disk is signaled by the rapid rolloff of the apparent surface brightness to an $\sim R^{-4}$ power law (even steeper than this for the largest objects).

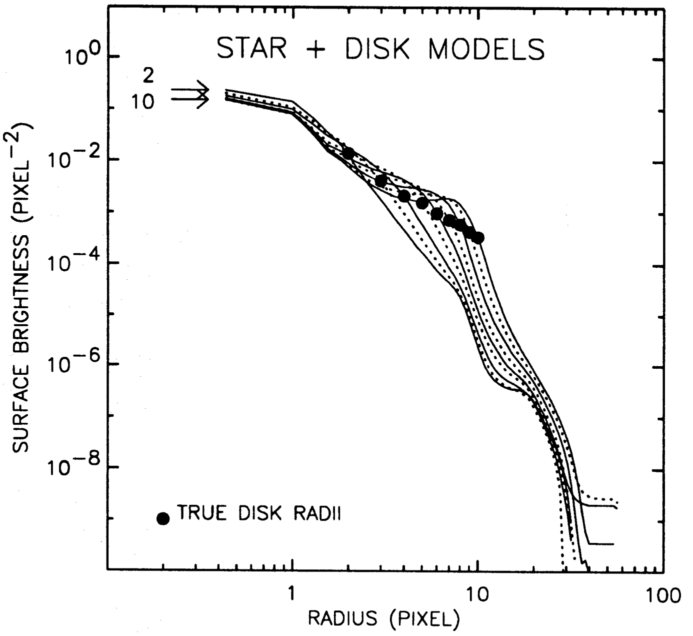

FIG. 6.—The reconstructed radial surface brightness of images of uniform, noise-free model nebular disks containing a central star of the same flux as the nebula after 100 iterations of the RL algorithm. Again, the point at which the surface brightness rolls off to a steep power law with radius provides a robust estimate of the true radius of the disk. However, in these cases, it is difficult to measure this point when the nebular radius is much less than ~2.5 PC pixels corresponding to a nebular diameter of about ~0.05 pc at the distance of the LMC.

## 4. RESULTS OF DECONVOLUTIONS

### 4.1. *Effect of PSF Mismatches*

The results presented above demonstrate that $\sim 100$ iterations represent the ideal compromise between resolution of any central object and optimal photometric veracity in its surrounding nebula. However, we still need to estimate the residuals expected when deconvolving a point source. These would result largely from the subsampling of the image inherent in the PC. As stated earlier, we only used two of the three PSF-STAR exposures to create our PSF for deconvolution purposes, thanks to an *HST* reacquisition event that did not return the star in the third exposure to the same chip location as the previous two. Serendipitously, this permits us to calculate the residuals by deconvolving the third PSF-STAR exposure with the observed PSF derived from the other two. These residuals manifest themselves as the remnants of the rings and tendrils seen in the aberrated exposure. In the restored image, the remaining artifacts were found to be approximately 4 orders of magnitude fainter than the peak number of counts in the core, and $\sim 89\%$ of the total stellar flux is contained within the central 0″.1 of the image core.

### 4.2. *Restored Images*

The PN images, as observed and restored, are presented in Figure 7 (Plates 11–18). Note that the display scale covers 2 orders of magnitude below the peak except for very extended PNs, for which the scale extends only a factor of 30 below the peak. In all instances, we have tried to avoid showing any ambiguous structure at very low intensities resulting from PSF mismatches.

### 4.3. *Aperture Photometry*

The deconvolved images were analyzed using the Galaxy Aperture Surface Photometry (GASP) software package, originally written by M. Cawson for the Starlink suite of astronomical software, but which has been ported to Unix and used here within the IRAF environment. The GASP algorithm, originally written to perform aperture surface photometry on galaxy images, has been described elsewhere (Davis et al. 1985; Jedrzejewski 1987). Briefly, it attempts iteratively to fit ellipses of a specified semimajor axis to an image, varying the ellipticity and position angle, but holding the ellipse center fixed, so as to minimize residuals about the mode of the pixel values around the perimeter of the ellipse, or else within elliptical annuli. The software uses a variation on the technique of Fourier descriptors in order to characterize deviations from a perfect ellipse and to identify which of the parameters (ellipticity or position angle) is most in need of adjustment. When a satisfactory fit is achieved, it repeats the process for a set of logarithmically increasing ellipse radii until either the sky background is reached, or until less than 60% of the ellipse will fit on the image.

In fitting ellipses to our PNs, we have determined the center of the PNs by eye and constrained the fitting procedure to center the ellipses at this point. Fitting ellipses to our PNs is clearly not appropriate in some cases, but this procedure delivers an objective estimate of the outer boundary of the PNs and in many cases enables us to estimate accurately the inclination of any ringlike feature which they may contain.

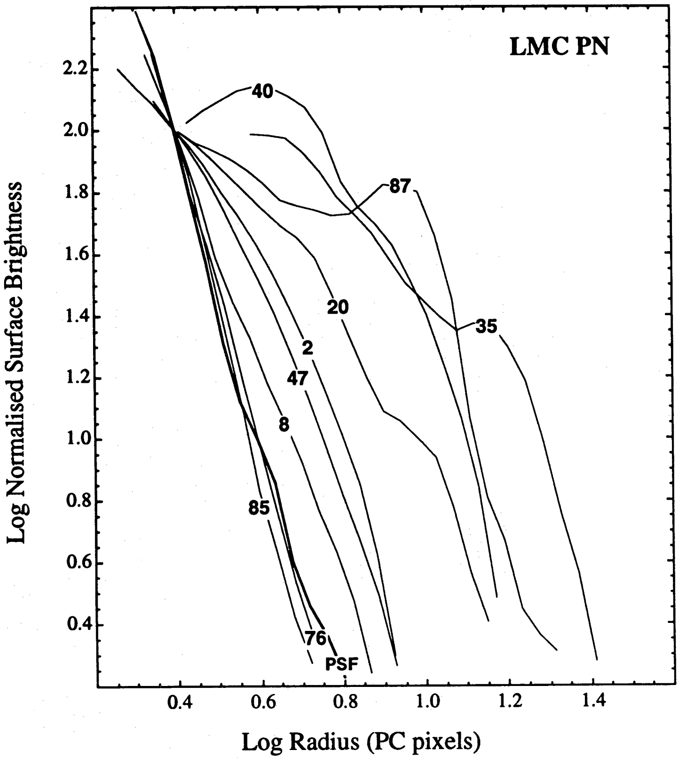

FIG. 8.—The results of GASP surface photometry on the restored LMC PN images shown in Fig. 8. All radial profiles have been normalized at 2.5 PC pixels to aid intercomparison. LMC-SMP 76 and 85 are too compact (and/or their extended regions are too faint) to be resolved. These profiles share many characteristics of the models in Figs. 6–7, and sizes can be estimated from the point at which the radial run of surface brightness rolls off into the steep outer power law which is an artifact of the residuals in the deconvolution process.

This process was applied to each of the images to derive the radial variation of surface brightness, the ellipticity, and the percentage of the integrated flux enclosed within the semimajor axis radius, $R$. In Figure 8 we show the radial profiles of the (deconvolved) PSF and the LMC PN, and in Figure 9 we show the corresponding profiles for the SMC PNs. Here the intensity scales have been normalized to 100 at a radius of 2.5 PC pixels to enable a simpler comparison of the radial profiles. SMP 76 and 85 are essentially unresolved, while SMP 8 shows evidence for a resolved halo around a central unresolved source. Nonetheless, all these three unresolved, or marginally resolved, images are still dominated by [O III] emission rather than being simply an image of the central star. By contrast, SMP 2, 20, 35, 40, and 87 in the LMC and SMP 3 in the SMC are extremely well-resolved PNs. Note how in all cases, the profile rolls over to the steep radial power law ($\sim R^{-4}$) in the outer regions, which is expected on the basis of our models when we pass beyond the true outer radius of the PN disk. This behavior is therefore an artifact of the deconvolution.

From our GASP photometry, we have derived two estimates of the outer diameter of the $D(85\%)$, the radius within which 85% of the total flux is to be found, and $D(\text{edge})$, the diameter at which the surface brightness rolls off to the steep outer power law. Other photometric features such as shell-like or ringlike structures are also to be found inside this outer radius, but our estimates of the outer diameter are reasonably robust and are likely to be a better estimate of the true diameter of the $\mathrm{O}^{++}$ Strömgren sphere, $D(\text{theor})$. The derived values of $D(85\%)$ and $D(\text{edge})$ are given in Table 3.

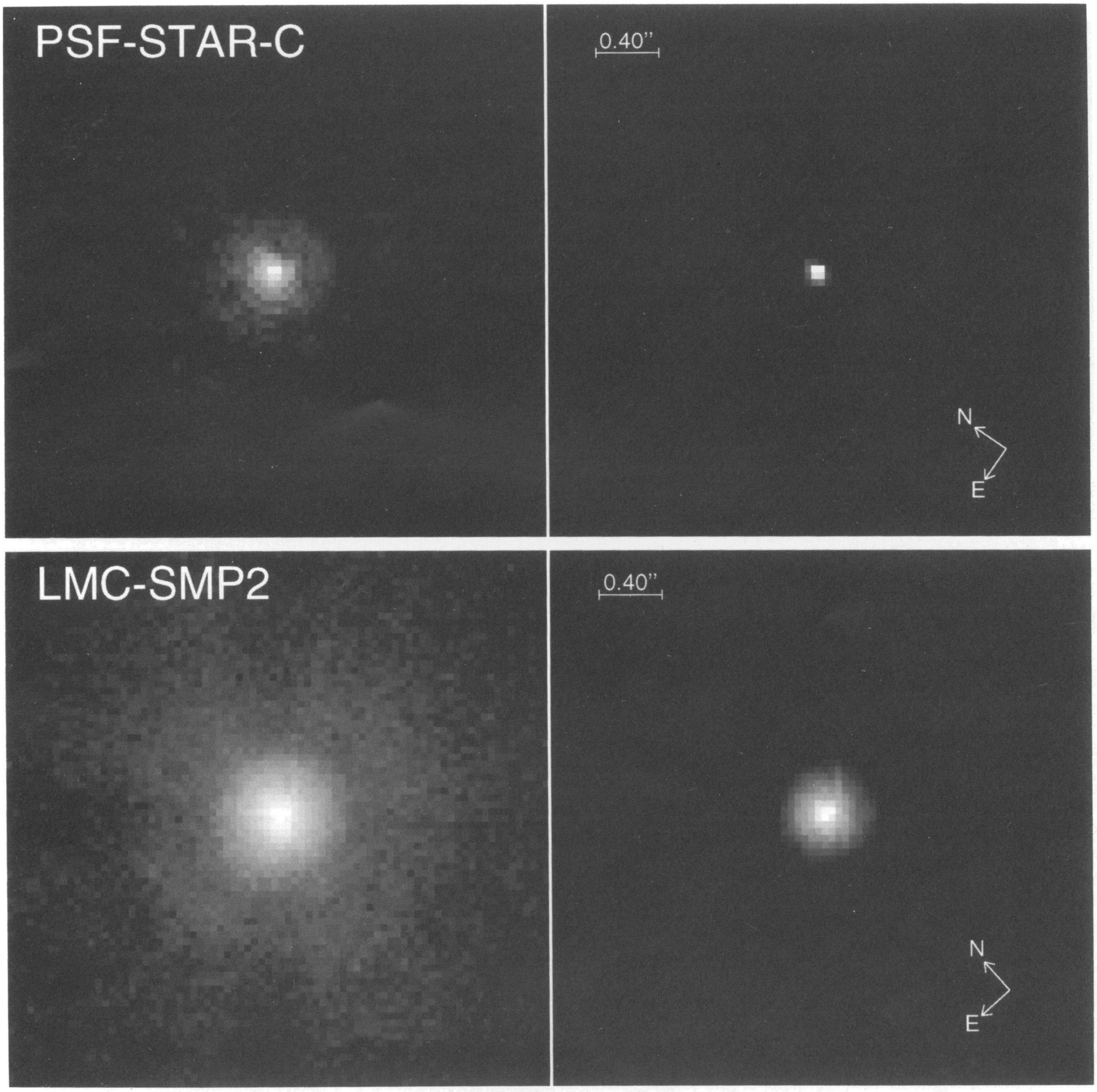

FIG. 7.—The reconstructed images of the Magellanic Cloud PNs. Note the predominance of bipolar morphology amongst the well-resolved PNs. In particular, *all* the type I objects display this characteristic. The LMC objects, SMP 20, 87, and 96, all show the classic "butterfly" morphology, but the faintest portions of the outlying wings are lost.

DOPITA et al. (see, 460, 327)

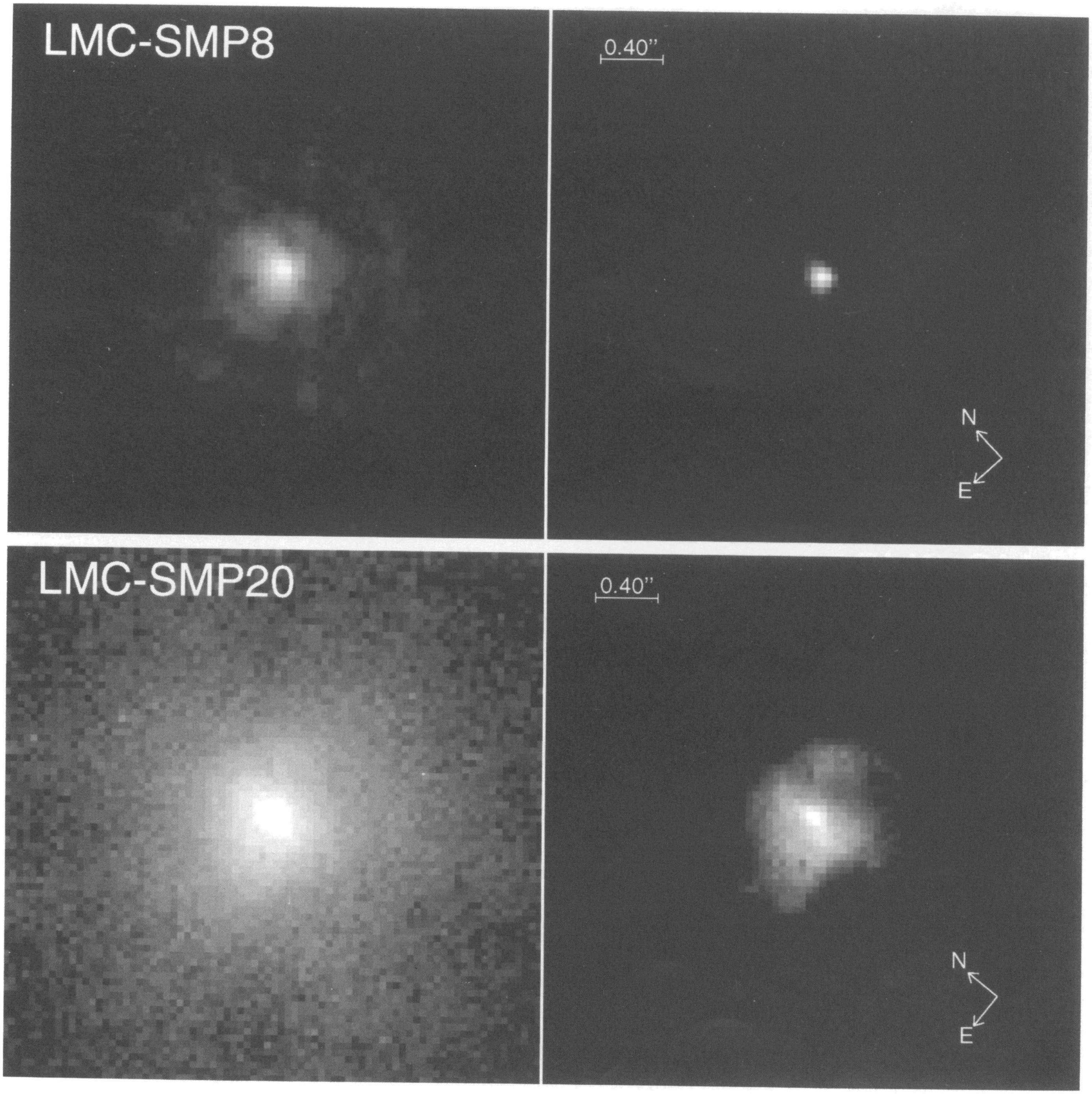

FIG. 7.—*Continued*

DOPITA et al. (see, 460, 327)

1996ApJ...460..320D

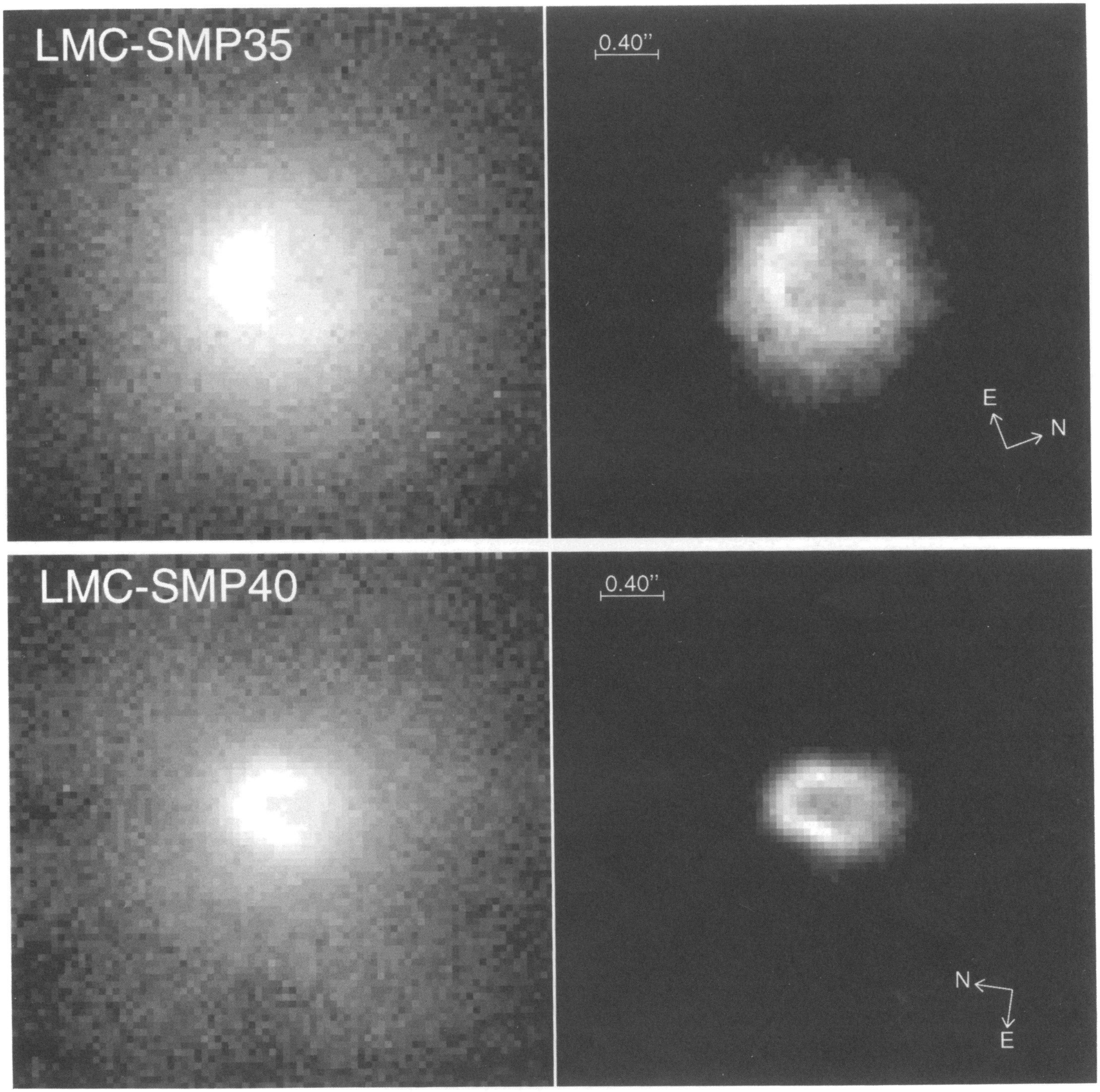

FIG. 7.—*Continued*

DOPITA et al. (see, 460, 327)

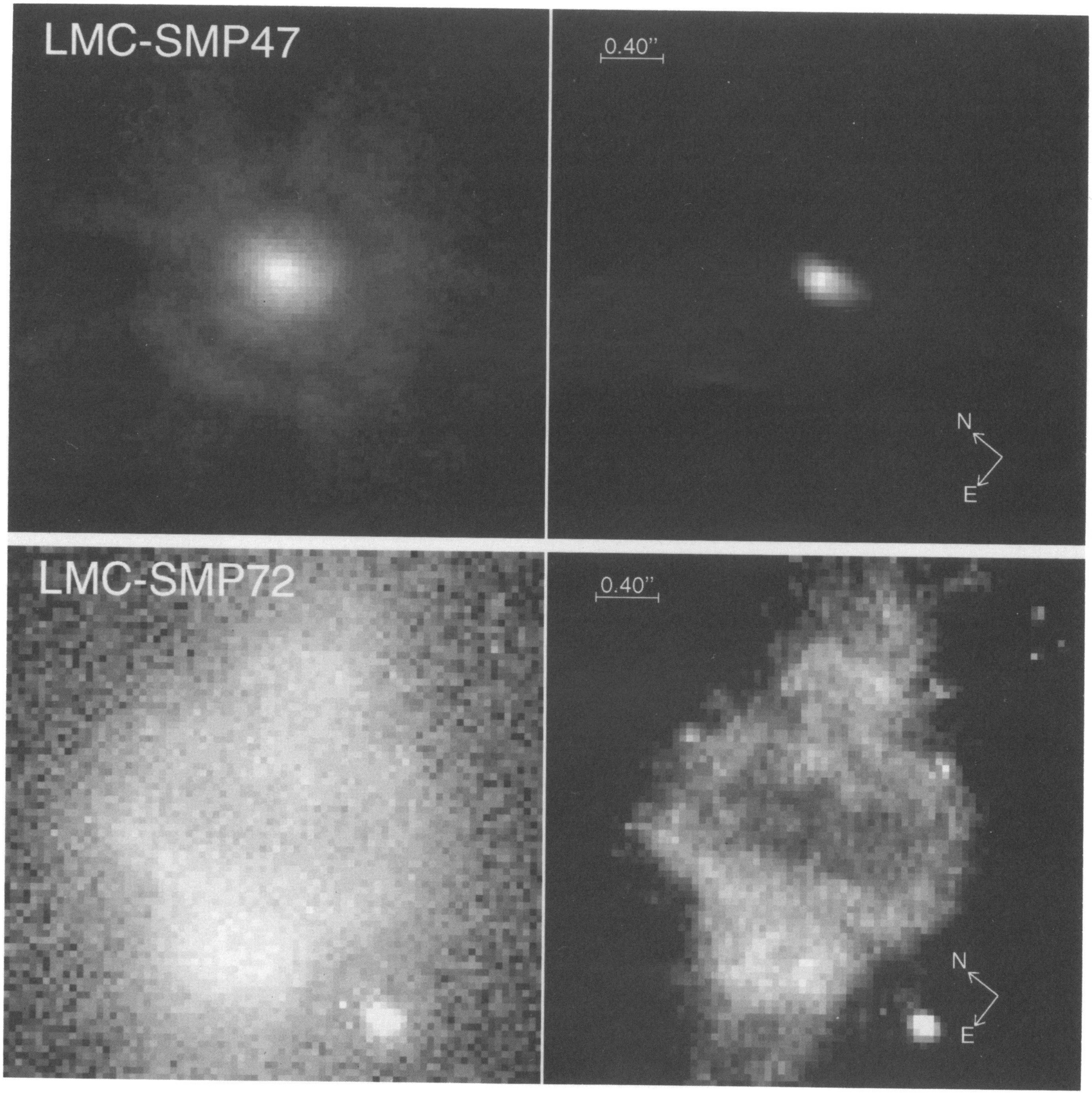

FIG. 7.—*Continued*

DOPITA et al. (see, 460, 327)

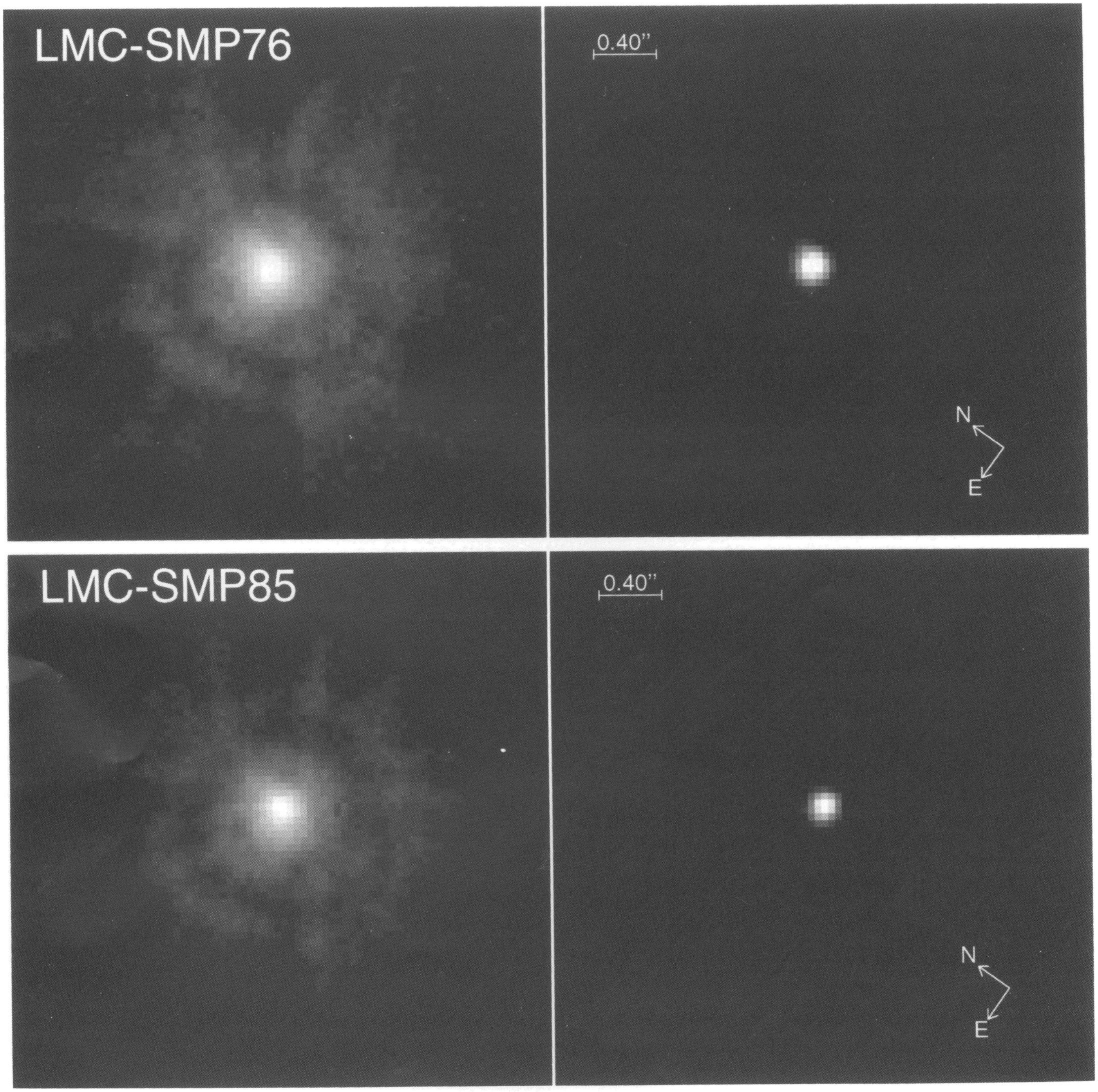

FIG. 7.—*Continued*

DOPITA et al. (see, 460, 327)

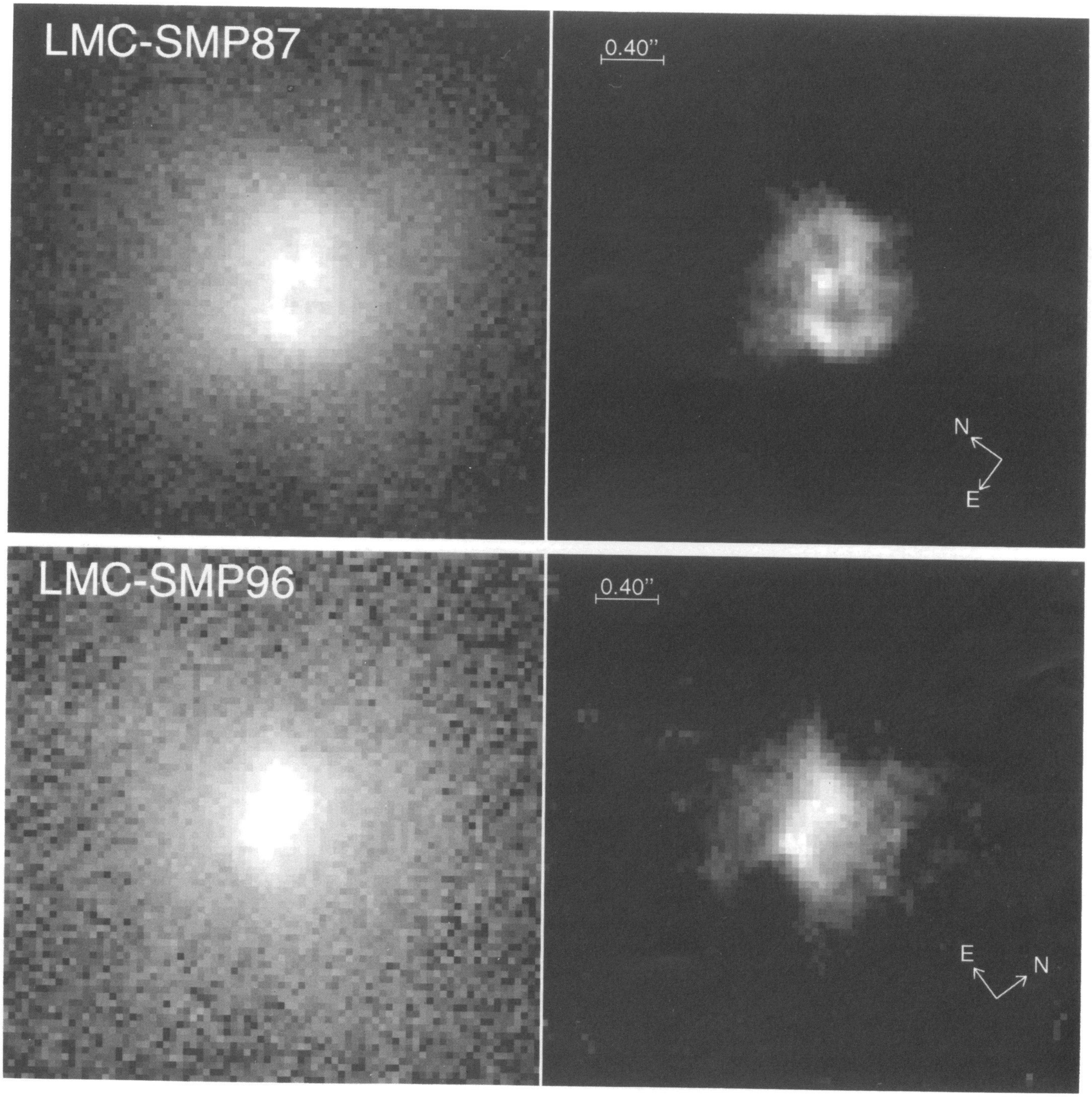

FIG. 7.—*Continued*

DOPITA et al. (see, 460, 327)

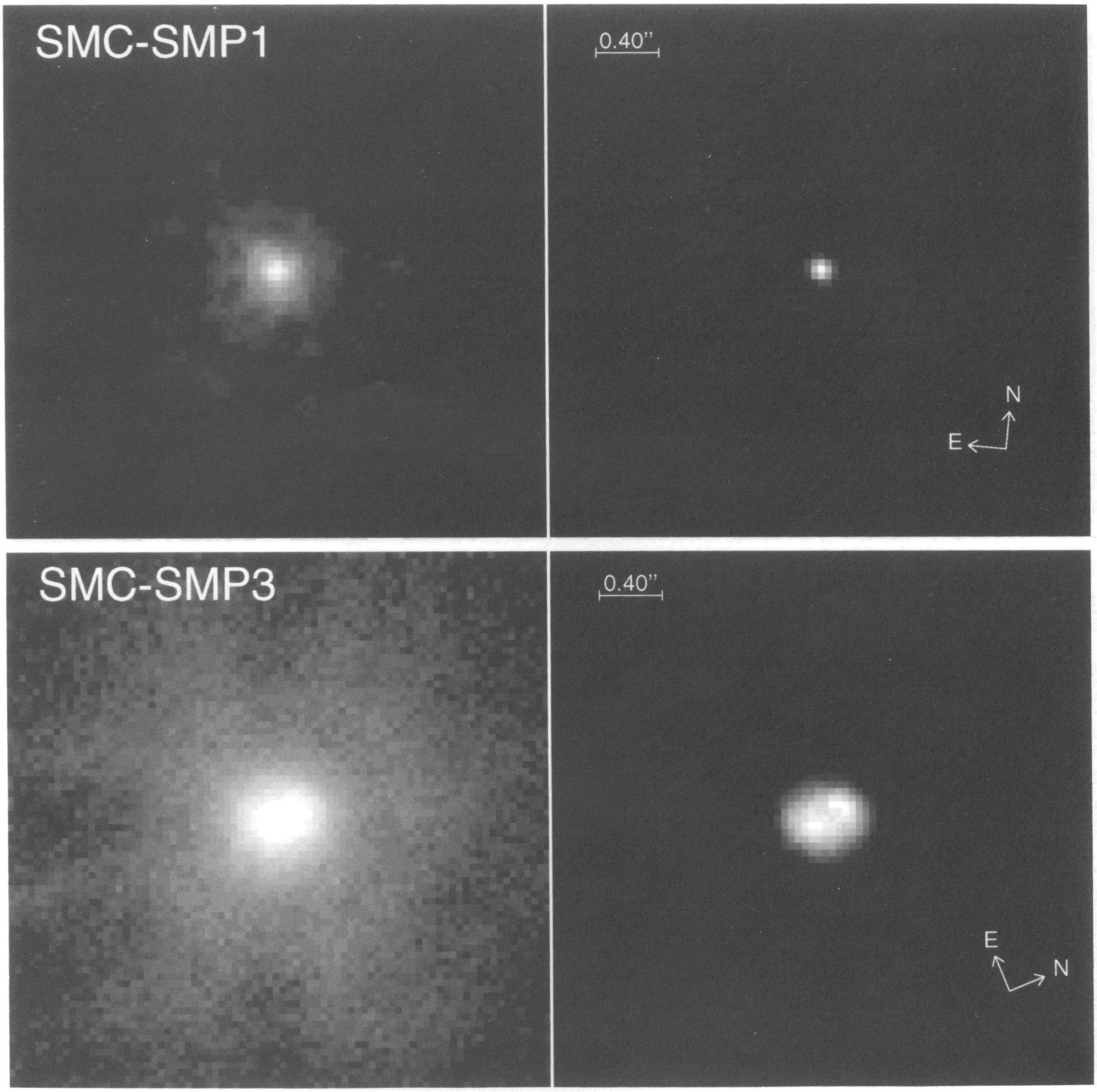

FIG. 7.—*Continued*

DOPITA et al. (see, 460, 327)

1996ApJ...460..320D

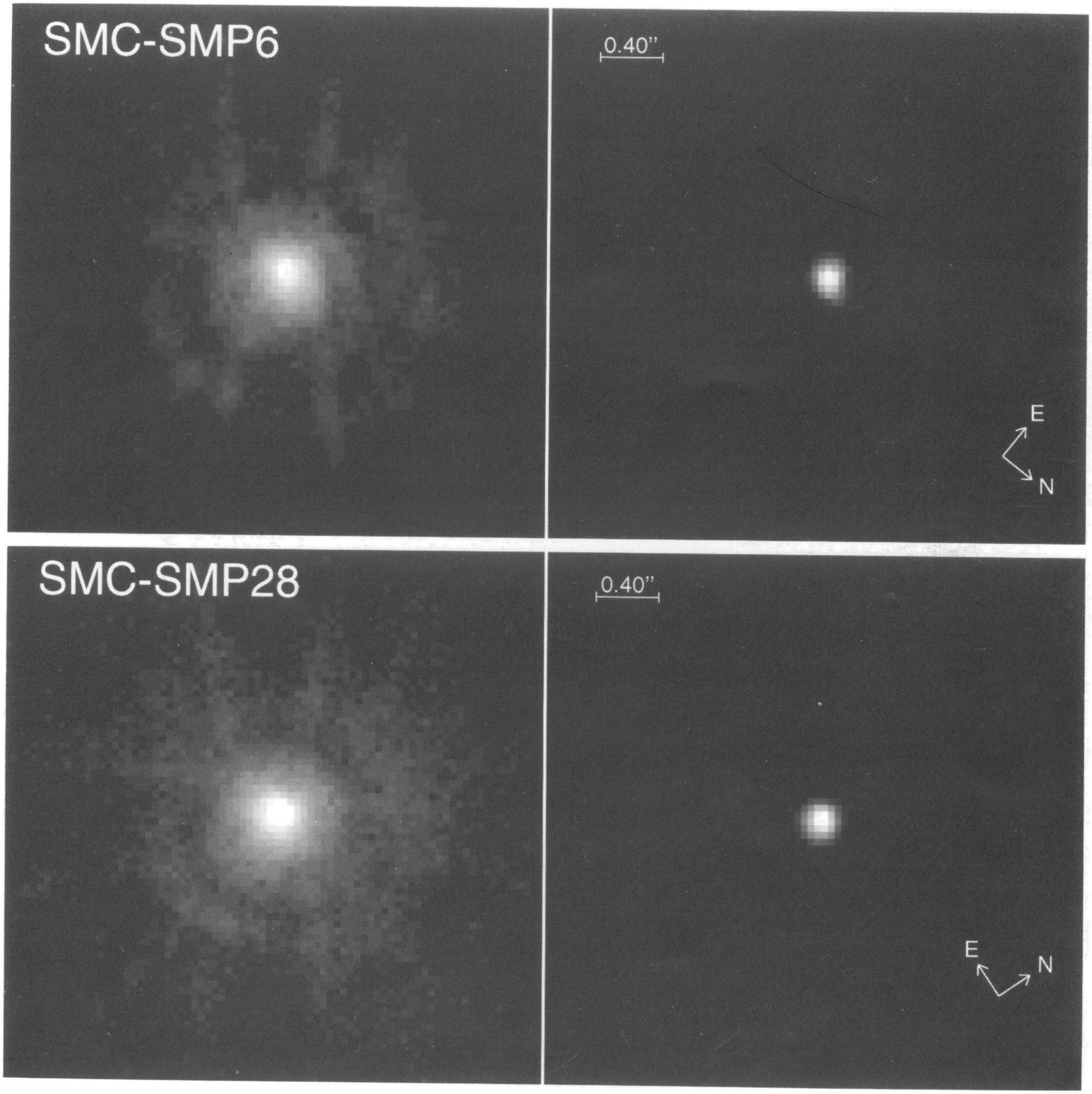

FIG. 7.—*Continued*

DOPITA et al. (see, 460, 327)

1996ApJ...460..320D

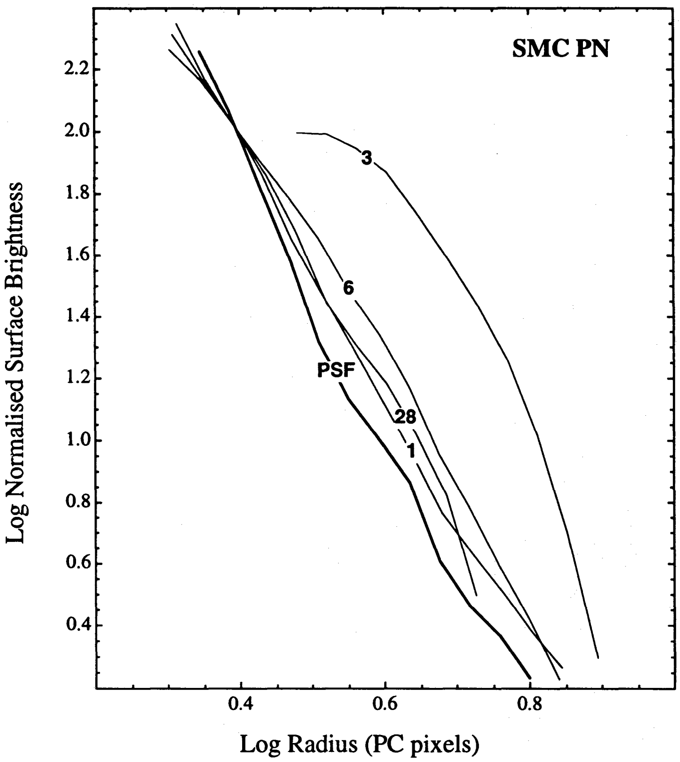

FIG. 9.—Same as Fig. 8, but for the SMC PNs

Finally, we have estimated by hand on the original images the ratio of semiminor to semimajor axis $q$ of any bright ringlike feature appearing within the image. Such structures are very apparent in LMC-SMP 20, 35, 40, 47, 72, 87, and 96 and in SMC-SMP 3. This then allows us to estimate the inclination, $\theta$, of the ring with respect to the plane of the sky; $\theta = \cos^{-1} q$. This parameter is given in Table 3 and is an important parameter in estimating the dynamical age, as is shown in the next section.

## 5. DYNAMICAL AGES

A major motivation for obtaining high-resolution images of these planetary nebulae is to be able to derive a dynamical age. This age is indicative of the time since the PNn evolved off the AGB. However, both the definition and the significance of such ages remains somewhat uncertain. If the nebula was a perfect expanding spherical ball of gas, the dynamical age would be simply defined by the ratio of measured nebular radius in the plane of the sky to the expansion velocity measured in the radial direction:

$$T_{\rm dyn} = R_{\rm neb}/V_{\rm exp} . \quad (5.1)$$

However, many PNs, particularly the nitrogen-rich type I objects, display a ringlike morphology with bipolar extensions. If what we measure as an expansion velocity is in fact the projection onto the radial direction of the true expansion velocity of the ring, then we have to correct the expansion age taking into account the fact that only a portion of the true expansion velocity maps into the radial velocity direction. For a ring with measured semiminor to semimajor axis ratio $q$, the true dynamical age is given by

$$T_{\rm dyn} = (1 - q^2)^{1/2} R_{\rm neb}/V_{\rm exp} , \quad (5.2)$$

where $V_{\rm exp}$ is the measured radial velocity of expansion.

On the other hand, in these cases, the velocity which is measured may well be the velocity of the bipolar outflow, in which case the dynamical age is then the dynamical age of the bipolar lobes. If $R_{\rm out}$ is the radius of these lobes projected onto the plane of the sky, and $q$ has the same meaning as before, then the dynamical age of the PNs is approximately

$$T_{\rm dyn} = (1 - q^2)^{1/2} R_{\rm out}/q V_{\rm exp} . \quad (5.3)$$

Experience with Galactic PNs teaches us that bipolar PNs are characterized by bipolar outflow along the long axis, so equation (5.3) is probably the better estimate of dynamical age. However, for objects with a central supply of unionized

TABLE 3

INFERRED TYPES, MORPHOLOGICAL CLASSES, DIAMETERS, INCLINATION ANGLES, AND DYNAMICAL AGES

| | | | Diameter (pc) | | | | | $T_{\rm dyn}$ (yr) | |
|---|---|---|---|---|---|---|---|---|---|
| Object | Excitation Class and Type | Morphological Class[a] | $D$(85%) | $D$(edge) | $D$(theor) | $V_{\rm exp}$ (km s$^{-1}$) | $\theta$ (deg) | Eqs. (5.1)–(5.2)[b] | Eq. (5.3)[c] |
| | | | | LMC PNs | | | | | |
| SMP 02...... | 1.1 | S | 0.100 | 0.133 | 0.067 | 9.9 | ... | 4910 | ... |
| SMP 08...... | 2.5 Thin? | S | <0.07 | 0.121 | 0.130 | 25.2 | ... | <1350 | ... |
| SMP 20...... | 8.1 Type I | Bc | 0.202 | 0.215 | 0.200 | 25.8 | ... | 3470 | ... |
| SMP 35...... | 5.4 | BR | 0.345 | 0.274 | 0.188 | 41.3 | 35 | 2330 | 1080 |
| SMP 40...... | 7.6 | R | 0.192 | 0.215 | 0.211 | 54.5 | 50 | 1310 | 2310 |
| SMP 47...... | 6.8 Type I | Bc | 0.101 | 0.139 | 0.149 | 78.7 | 60 | 540 | 1490 |
| SMP 72...... | 8.5 Thin | BR | 0.470 | 0.371 | 0.361 | ... | 50 | ... | ... |
| SMP 76...... | 2.6 | S | <0.07 | <0.04 | 0.081 | 29.0 | ... | <1170 | ... |
| SMP 85...... | 1.5 | S | <0.07 | <0.04 | 0.037 | 11.3 | ... | <3010 | ... |
| SMP 87...... | 9.0 Type I | BR | 0.248 | 0.220 | 0.296 | 37.4 | 55 | 2640 | 4104 |
| SMP 96...... | 9.3 Type I | BR | 0.222 | 0.139 | 0.132 | 60.9 | 70 | 1650 | 1990 |
| | | | | SMC PNs | | | | | |
| SMP 01...... | 1.1 | S | 0.068 | 0.105 | 0.082 | 15.4 | ... | ... | ... |
| SMP 03...... | 5.0 Thin | BR | 0.122 | 0.145 | 0.187 | 32.9 | 45 | ... | ... |
| SMP 06...... | 3.8 | S | 0.086 | 0.100 | 0.070 | 21.9 | ... | ... | ... |
| SMP 28...... | 7.2 Type I | S | 0.075 | 0.100 | 0.187 | 54.4 | ... | ... | ... |

[a] Morphological classifications: S = spherical, Bc = bipolar, central condensation, BR = bipolar ring, R = ring.

[b] Calculated using eq. (5.1) for S type, and eq. (5.2) for Bc, BR, and R types.

[c] Calculated using eq. (5.3) for Bc, BR, and R types.

gas, the velocity which is measured more likely reflects the outflow velocity from the embedded ionization fronts and so has little to do with the true dynamical age.

In Table 3 we give the expansion velocities from Dopita et al. (1985, 1988). These velocities were measured for the [O III] $\lambda$5007 line and are therefore directly applicable to these observations. They were defined at 10% of maximum line intensity and are therefore a measure of the fastest moving plasma along the line of sight. In order to arrive at this value of 10%, we performed extensive modeling of different PN geometries. The 10% flux level appeared to be the point at which we could measure an edge expansion velocity which was largely independent of details of the brightness distribution in the nebula. Therefore, it is appropriate to use the outer radii found from the imaging, and therefore we have used $R_{\rm neb} = D(85\%)/2$ and $R_{\rm out} = D(\rm edge)/2$ for substitution into equations (5.1)–(5.3). The inferred dynamical ages are given in Table 3. These range from less than 1000 years up to nearly 5000 years and are in general shorter than the theoretical ages for the PNn's. This somewhat puzzling result and its interpretation are discussed in the following section.

## 6. DISCUSSION

### 6.1. *Comparison with Theoretical Sizes*

In Figure 10 we compare the sizes of the $O^{++}$ zone given by the two estimates of the diameter with those derived from the Dopita & Meatheringham (1991a, b) photoionization models. For comparison, the line of equal diameters is also shown. The observational edge and the shell diameters both agree reasonably well with those predicted by the models. The correlation coefficient between the theoretical diameter and $D(85\%)$ is 0.65, and the correlation coefficient between the theoretical diameter and $D$(edge) is 0.74. The most compact objects generally tend to be more compact than simple photoionization models would predict. However, we know from our photometric tests that faint nebular extensions or compact nebular disks will both tend to be lost in objects with a condensed central nucleus. This appears to be the case for LMC-SMP 76 and LMC-SMP 85, SMC-SMP 1, and SMC-SMP 28. To a lesser extent, it is also true for LMC-SMP 8 and SMC-SMP 6. Nonetheless, our test models show that a compact nuclear object cannot appear as an artifact of the deconvolution. It must really exist, although it may not be as bright as the deconvolution suggests.

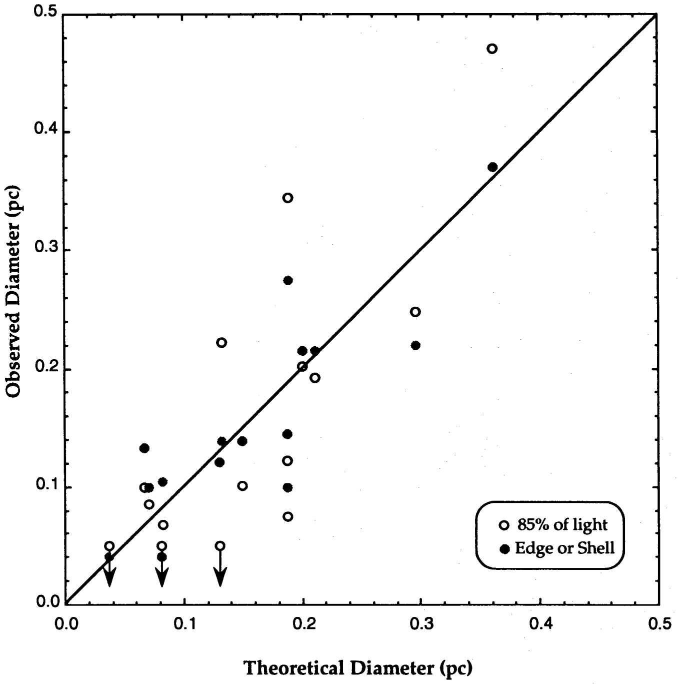

FIG. 10.—A comparison of the sizes of the PNs inferred from the images, and the sizes expected on the basis of photoionization models using ground-based data (from Dopita & Meatheringham 1991a, b). There is generally speaking a good correspondence between the observations and theory. The smallest objects tend to be measured to be smaller than theory would predict, but at least some of this effect is attributable to the artifacts of the deconvolution procedure in the presence of a bright central object.

Table 3 shows that the unresolved or partially resolved PNs tend to be low-excitation objects. However, the equivalent width of the [O III] $\lambda$5007 line with respect to the stellar continuum is in all cases greater, and in most cases much greater, than the equivalent width of the filter ($\sim$15 Å). Therefore, we cannot ascribe the central condensation to the dominating presence of a central star. The dense central condensation is therefore a nebular, rather than a stellar, feature. It presumably traces the internal ionization fronts around a dense, unionized structure close to the central star.

In the case of LMC-SMP 85, Dopita et al. (1994) have already shown the need for a dense reservoir of unionized gas to provide a satisfactory model to both the inferred size and the observed emission-line spectrum. In fact, the reanalysis of the image presented here would probably require a model which is even more extreme than that presented in that earlier paper.

The presence of such a dense central condensation is a little surprising and suggests that the final evolution off the AGB may be characterized by a "superwind" episode of short lifetime and of very low expansion velocity. It is tempting to associate this with a final helium shell flash.

### 6.2. *Evidence for Evolution on the H-R Diagram*

In Figure 11 we show the images of the LMC PNs plotted at the same spatial scale and at their correct positions on the H-R diagram derived from photoionization modeling based on ground-based spectrophotometry (Dopita & Meatheringham 1991a, b). Clearly there is size evolution along the evolutionary tracks, in the sense that objects which fall on the fading portions of the evolutionary tracks are all physically larger than the cooler, low-excitation objects.

Somewhat surprisingly, however, no clear trends emerge connecting the dynamical age with any other evolutionary parameters such as position on the H-R diagram. Nonetheless, some conclusions may be drawn with respect to individual objects. In particular, the age of LMC-SMP 2 is large and is clearly much greater than either SMP 8 or SMP 85. This is consistent with evolutionary models in which the rate of evolution across the H-R diagram is critically dependent on the core mass, low-mass PNs taking much longer to move to higher temperatures. However, the position on the H-R diagram inferred from the photoionization models for LMC-SMP 2 is below the lowest mass evolutionary track consistent with H-burning stars according to the models of Vassiliadis & Wood (1993). Thus, LMC-SMP 2 is constrained to be a He-burning object.

Overall, the lack of any clear correlation of dynamical age and position on the H-R diagram might result from the

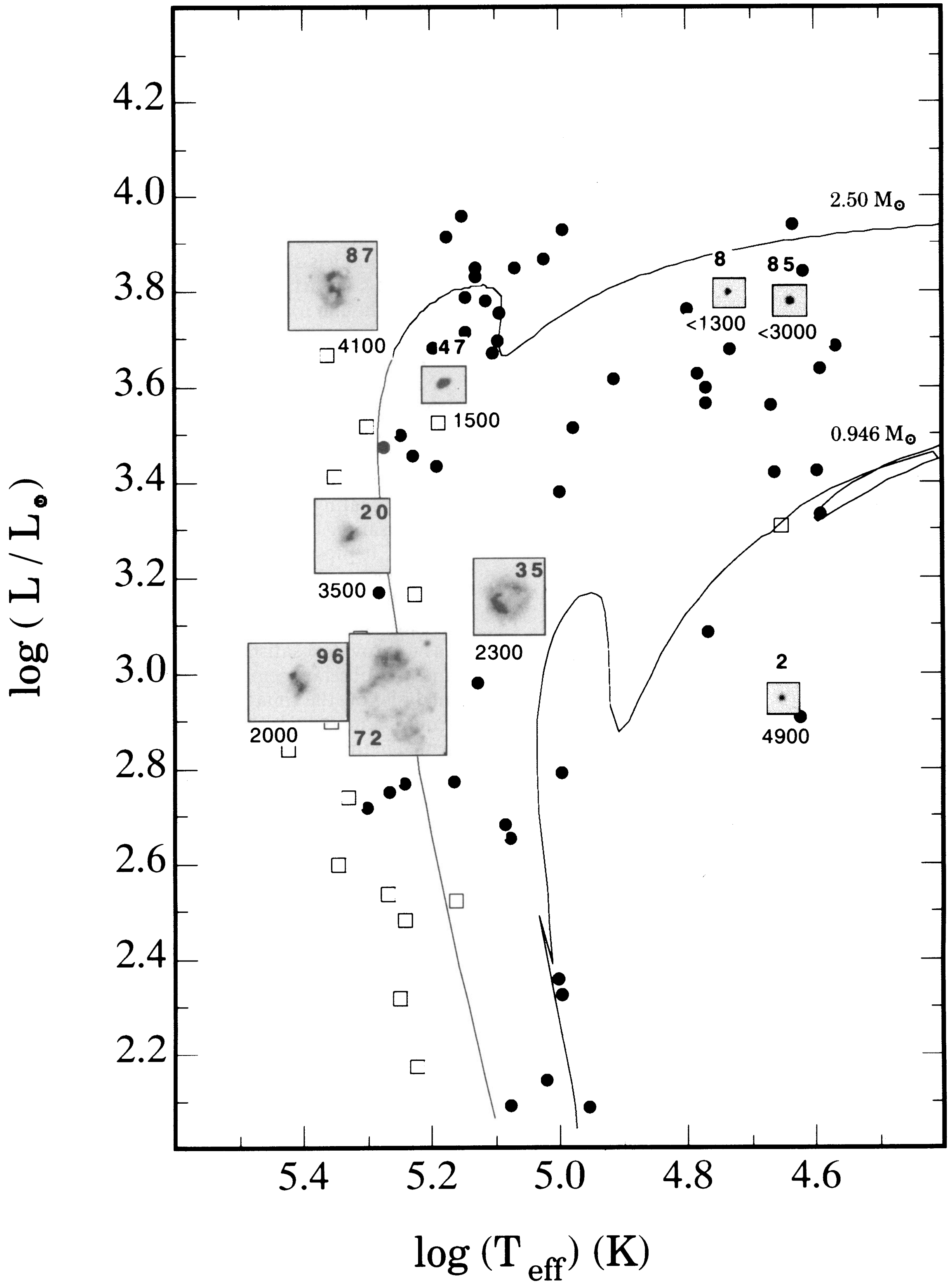

FIG. 11.—The images of the LMC PNs are superimposed here on the observational H-R diagram from Dopita & Meatheringham (1991b). Each image is presented at the same scale and at the point on the H-R diagram indicated by its photoionization model. The dynamical age in years is given for each of the objects. For comparison, two helium-burning tracks from Vassiliadis & Wood (1993) are shown, along with their initial stellar mass. There is clear evidence for a size evolution along the evolutionary tracks, but the evidence for a corresponding increase in dynamical age is much weaker.

dynamical evolution of the PN nebular shells themselves. A general correlation between the excitation class and expansion velocity was found by Dopita et al. (1988). In general, excitation class tracks closely to the logarithm of the effective temperature (Dopita & Meatheringham 1991a). Subsequently (Dopita 1993), it was found that an even closer correlation existed between a combination of log $(L/L_{\odot})$, log $(T_{\rm eff})$, and expansion velocity:

$$(V_{\rm exp}/{\rm km\ s^{-1}}) = -128 \pm 4 + 38 \pm 2[\log (T_{\rm eff}) - 0.25 \pm 0.05 \log (L/L_{\odot})] . \quad (6.1)$$

Equation (6.1) implies that the expansion velocity of LMC-SMP 72 should be 44 km $s^{-1}$, giving a dynamical age in the range 4000–5000 yr for this object.

It is clear that the empirical relation (6.1) is fundamental to our understanding of the dynamical evolution of PNs. It shows that the PN shells are accelerated continuously during the evolution of the PNn toward the blue. This acceleration occurs early for low-mass PNs, but higher terminal velocities are reached in the case of the high-mass PNs. This is consistent with a lower shell mass in the low-mass PNs and more energetic stellar winds in the high-mass PNs.

Apparently then, the PN shells are initially accelerated by the increase of thermal energy content during their nuclear-burning phase of evolution, and they coast at constant expansion velocity during the fading track. In this model, the stellar wind provides the pressure which confines the ionized material to a (somewhat) thin shell. The terminal velocity reached by the nebular shell is correlated with the mass of the PNn: more massive PNn's driving faster expansion. The increase in thermal energy content is in part caused by the increase in ionized mass but is mostly attributable to thermalization of the fast stellar wind which develops as the PNn tracks to high temperatures on the H-R diagram. In this case, the dynamical age of old PNs will be closer to the time since the acceleration phase of the PN shell rather than reflecting the true age since the PNn left the AGB. A further implication of the observational relation (6.1) is that old PNs in the Magellanic Clouds do not show any late deceleration in their expansion as a result of interaction with the interstellar medium (ISM) before the PN itself has finally faded below the sensitivity limit of the SMP survey. However, it remains possible that fainter PNs, such as those studied by Jacoby & Kaler (1993), may show such an effect.

From this discussion, it is clear that the concept of dynamical age as currently applied to PNs is too simplistic and will always be an underestimate of the true age since the PNn left the AGB. In order to provide a critical dynamical test of PN evolution, we require evolutionary models of the PNn to be linked to dynamical models for the PN itself.

### 6.3. *Derivation of Evolutionary Ages*

We can derive a true evolutionary age for the PNs semiempirically as follows. Equation (6.1) gives the velocity of expansion in terms of the parameters of the H-R diagram. However, the models of Vassiliadis & Wood give the rate of evolution of the PNs across the H-R diagram. We can therefore combine equation (6.1) with the evolutionary models to determine an equation of motion which can then be integrated to find the theoretical radius of the PNs for each central star. To do this, we assume that the PN shell is ejected at a minimum velocity of 5 km $s^{-1}$, about equal to the minimum of the observed expansion velocities. We also assume that the PNn evolves rapidly from the point at which it leaves the AGB to the point at which the central star temperature exceeds $10^4$ K. The evolution of the PNn depends critically upon whether the central star is He or H burning. H-burning PNs are on average more luminous than their He-burning counterparts. However, the time available for acceleration of the PN shell tends to be short for the more massive H burners. These factors compete in determining the radius-age relation. This is shown in Figures 12*a*–12*b*. The H burners show a large scatter in this figure as a function of the initial mass of the central star, whereas the He burners follow a relationship with quite small scatter.

We can use the position of the PNn on the H-R diagram as inferred from the Dopita & Meatheringham (1991a, b) photoionization models in conjunction with the evolution-

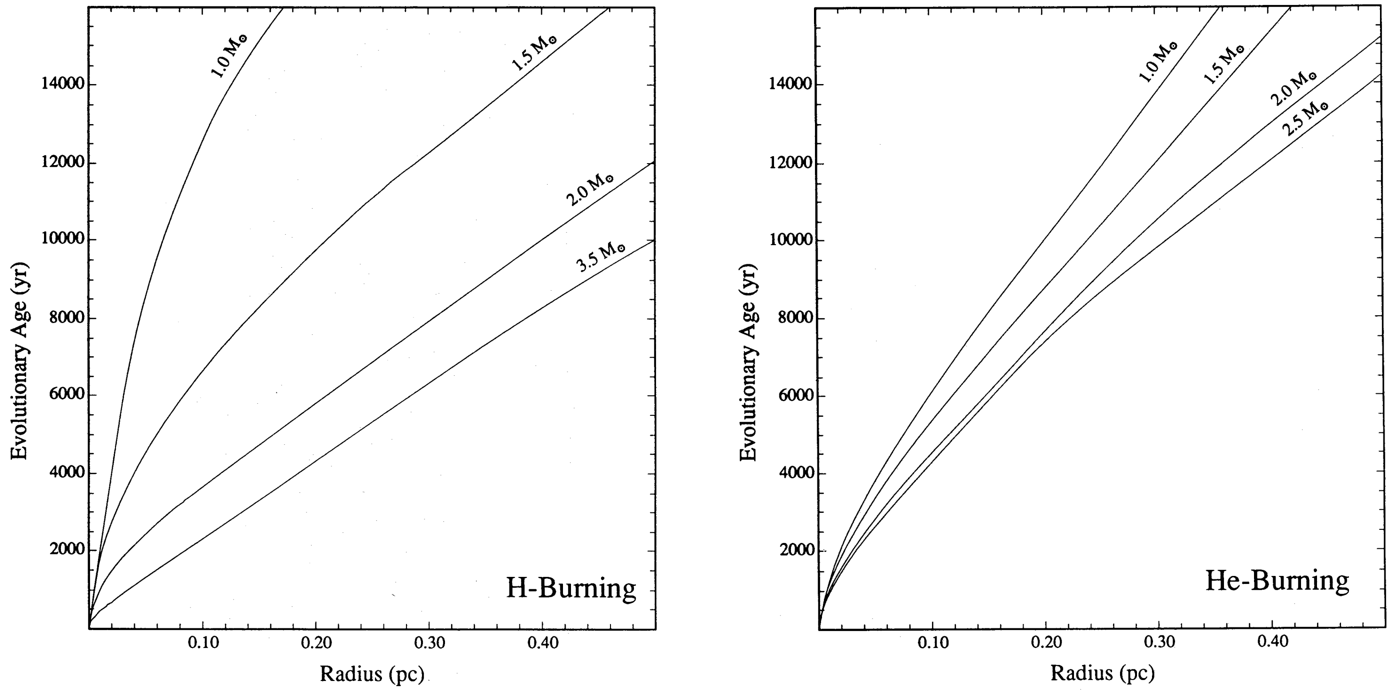

FIG. 12*a*

FIG. 12*b*

FIG. 12.—The radius–evolutionary time relationship for PNs for (*a*) H-burning PNn's and (*b*) He-burning PNn's. This is derived using the semiempirical equation of motion (6.1) and the Vassiliadis & Wood (1992) evolutionary models.

1996ApJ...460..320D

TABLE 4

INFERRED POSITIONS ON THE H-R DIAGRAM, RADII, AND AGES OF LMC PNs COMPARED WITH THEORY

| OBJECT | log $T_{\rm eff}$ | log $L/L_\odot$ | $R$ (pc) | DYNAMICAL AGES (He-BURNING) | | | DYNAMICAL AGES (H-BURNING) | | | PN TYPE |
|---|---|---|---|---|---|---|---|---|---|---|
| | | | | $t_{\rm R}$ | $t_{\rm Ev}$ | $t_{\rm H\text{-}R}$ | $t_{\rm R}$ | $t_{\rm Ev}$ | $t_{\rm H\text{-}R}$ | |
| SMP 02...... | 4.620 | 2.910 | 0.058 | 4500 | 6500 | 9000 | >10000 | 9000 | Indefinite | He |
| SMP 08...... | 4.720 | 3.750 | ~0.043 | 3000 | <2000 | 1500 | 4000 | <2000 | 4500 | H/He |
| SMP 20...... | 5.310 | 3.100 | 0.104 | 4500 | 5000 | 6500 | 2500 | 6000 | 650 | He |
| SMP 35...... | 5.070 | 3.170 | 0.154 | 8500 | 1500 | 35000 | 15000 | 6000 | 29000 | H |
| SMP 40...... | 5.270 | 3.040 | 0.102 | 4500 | 3000 | 9500 | 4000 | 5700 | 3200 | H |
| SMP 47...... | 5.180 | 3.610 | 0.060 | 3000 | 2000 | 10000 | 3000 | 2500 | 3000 | H |
| SMP 72...... | 5.250 | 2.960 | 0.210 | 8000 | ... | 9500 | 6000 | ... | 3000 | He |
| SMP 76...... | 4.720 | 3.850 | <0.027 | <2000 | <1500 | 1200 | <1000 | <2000 | 2500 | He |
| SMP 85...... | 4.610 | 3.820 | <0.027 | <2000 | <4000 | 650 | <2500 | <4000 | 2000 | H/He |
| SMP 87...... | 5.350 | 3.810 | 0.117 | 5000 | 5000 | 6000 | 7000 | 6500 | 1500 | He |
| SMP 96...... | 5.340 | 2.970 | 0.090 | 3500 | 3000 | 5000 | 3000 | 3500 | 650 | He |

ary tracks of Vassiliadis & Wood (1993) to estimate the initial main-sequence mass of the PNn on the assumption either that it has an H-burning or that it has a He-burning central star. With this mass, and using the observed radius given in Table 3, we can then read off the evolutionary age implied from Figure 12. In order to reduce scatter, we have taken the radius as $[D(85) + D(\text{edge})]/4$. In Table 4 we give the resulting evolutionary timescales for the LMC planetary nebulae based on the radius, $t_R$.

An alternative approach to the problem is to correct the dynamical expansion ages given in Table 3 by a factor which accounts for the acceleration of the PN shell. This factor is given in Figure 13 for both the H burners and the He-burning stars. The dynamical age is derived from the semiempirical radius from Figure 12 divided by the expansion velocity given by the gradient of the radius-time relation at this radius. The correction factor is then the ratio of the true age to the dynamical age. For the He burners, there are two maxima on this relationship, the first corresponding to the initial acceleration phase of the PNs, and the second corresponding to the episode of hydrogen reignition, which enhances the stellar mass-loss rate and leads to a second episode of acceleration of the PN shell.

Having derived the mass track which is consistent with the position of the PNs on the H-R diagram, we can then read off the appropriate correction factor to the inferred dynamical age and thus derive the evolutionary timescales based on the dynamical timescale, $t_{\rm Ev}$.

Finally, we require that the timescales derived in this manner should be consistent with the time since the PNn left the AGB, as derived from the Vassiliadis & Wood (1993) evolutionary tracks, $t_{\rm H\text{-}R}$. This consistency check shows that in some objects, the timescales agree closely provided the central star is assumed to be H burning, and in others the agreement is found only if the central star is a He burner. This enables us to classify the PNn as either H-burning or

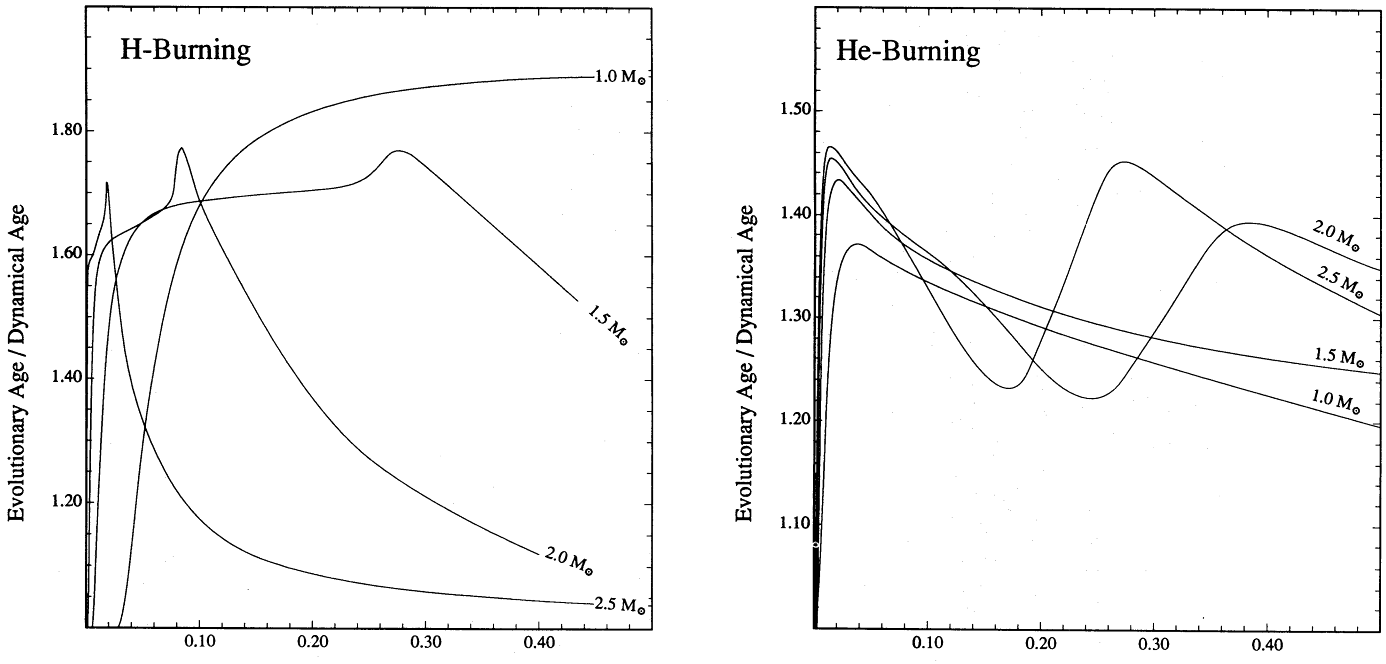

FIG. 13*a*

FIG. 13*b*

FIG. 13.—The correction factors that should be applied to derived dynamical ages in order to compute true evolutionary timescales for (*a*) H-burning PNn's and (*b*) He-burning PNn's. These are derived in the same way as the curves in Fig. 12.

He-burning. The probable classification of each PNn is given in the final column of Table 4. We find that six PNn's are likely to be He-burning, three are almost certainly H-burning, and two cannot be classified on this basis. Of the four type I objects, three are likely to be He burners.

Dopita Jacoby, & Vassiliadis (1993) claimed, on the basis of the distribution of PNn's on the H-R diagram, that the majority of PNn's in the LMC were He burners. This viewpoint is not one that has been generally accepted in the past (e.g., Schönberner 1983; Blöker & Schönberner 1990). However, Wood & Vassiliadis (1993) argued that at least 40% of the PNn's should be He-burning on the basis of the fraction expected to leave the AGB as a function of phase of the shell flash cycle, and taking into account the relative rates of evolution of the He and H burners across the H-R diagram. The (small number) statistics we have derived here suggest that ~45%–70% are He burners. This fraction could be easily accommodated within the theoretical expectations if the shell flash episode itself leads to a somewhat enhanced mass loss, causing the PNn to preferentially leave the AGB as a He-burning star.

The most interesting thing about Table 4 is that the evolutionary timescales derived agree rather well with the theoretical values. This is the first time that such a concurrence has been found in individual objects.

In the fifth paper in this series, we will extend the sample by the inclusion of cycle 3 imaging results and by use of the GTO images. This will nearly double the sample of PNs and will allow us to investigate, for example, the validity and universality of the empirical equation of motion, applied separately to the H-burning and He-burning objects.

## 7. CONCLUSIONS

From cycle I *HST* Planetary Camera images of PNs in the Magellanic Clouds deconvolved using 100 iterations of the Richardson-Lucy image restoration algorithm, we have been able to investigate both the size evolution and the morphological structure of these objects.

We find clear evidence for size evolution across the H-R diagram. The younger, low-excitation, compact planetary nebulae tend to be systematically smaller than photoionization models based on ground-based data would predict, suggesting that these planetary nebulae have a central reservoir of dense atomic and molecular gas lying close to the central star, undergoing ionization, and being accelerated into outflow. The nitrogen-rich objects with massive central stars (Peimbert type I) show the bipolar "butterfly" symmetry that is also a characterstic of their Galactic counterparts.

Using the empirical fit that we derived previously relating the expansion velocity to the position on the H-R diagram, and the theoretical evolutionary tracks of the central star, we have derived two semiempirical estimates for the evolutionary timescales. One of these is based only upon the nebular size, and the other is derived by correcting the measured dynamical age for the acceleration of the PN shell during its lifetime. We find that these evolutionary timescales are consistent with the evolutionary age derived from theory, provided that some PNs are H burning and others are He burning. From 11 objects in the LMC, we find that He burners outnumber H burners in the approximate ratio 2:1. In the fifth paper of this series, we will analyze cycle 3 images and images produced as part of the GTO program to approximately double the sample of PNs so studied.

The results presented here are based on observations with the NASA/ESA *Hubble Space Telescope*, obtained at the Space Telescope Science Institute, which is operated by the Association of Universities for Research in Astronomy, Inc., under NASA contract NAS5-26555. Support for this work was provided by NASA through grant number GO-2266 from the Space Telescope Science Institute. Australian collaborators wish to acknowledge travel support under a major grant from the International Science and Technology Division of the Australian Department of Industry, Science and Technology.

## REFERENCES

Baade, D., & Lucy, L. B. 1989, in Proc. 1st ESO/ST-ECF Data Analysis Workshop, ed. P. Grosbol, F. Murtagh, & R. Warmels (Garching: ESO) 169
Barlow, M. J. 1989, in IAU Symp. 131, Planetary Nebulae, ed. S. Torres-Peimbert (Dordrecht: Kluwer), 319
Baxter, D. A., Greenfield, P. E., Hack, W., Nota, A., Jedrzejewski, R. I., & Paresce, F. 1993, in Space Astronomical Telescopes and Instruments II, SPIE, vol. 1945, ed. P. Y. Bely & J. B. Breckinridge (SPIE), 252
Blades, J. C., et al. 1992, ApJ, 398, L41
Blöker, T., & Schönberner, D. 1990, A&A, 240, L11
Burrows, C. J., Holtzman, J. A., Faber, S. M., Bely, P. Y., Hasan, H., Lunds, C. R., & Schroeder, D. 1991, ApJ, 369, L21
Davis, L. E., Cawson, M., Davies, R. L., & Illingworth, G. 1985, AJ, 90, 169
Dopita, M. A. 1993, in IAU Symp, 155, Planetary Nebulae, ed. R. Weinberger & A. Acker (Dordrecht: Kluwer), 433
Dopita, M. A., Ford, H. C., Bohlin, R. C., Evans, I. R., & Meatheringham, S. J. 1993, ApJ, 418, 804 (Paper I)
Dopita, M. A., Ford, H. C., Lawrence, C. J., & Webster, B. L. 1985, ApJ, 296, 390
Dopita, M. A., Ford, H. C., & Webster, B. L. 1985, ApJ, 297, 593
Dopita, M. A., Jacoby, G. H., & Vassiliadis, E. 1992, ApJ, 389, 27
Dopita, M. A., & Meatheringham, S. J. 1991a, ApJ, 367, 115
———. 1991b, ApJ, 377, 480
Dopita, M. A., Meatheringham, S. J., Ford, H. C., & Webster, B. L. 1988, ApJ, 327, 651
Dopita, M. A., et al. 1994, ApJ, 426, 150 (Paper II)
Hasan, H., Burrows, C. J., & Schroeder, D. J. 1993, PASP, 105, 692
Henize, K. G. 1956, ApJ, 2, 315
Iben, I., Jr. 1984, ApJ, 277, 333
Jacoby, G. H. 1980, ApJS, 42, 1
Jacoby, G. H., & Kaler, J. B. 1993, ApJ, 417, 209
Jacoby, G. H., Walker, A. R., & Ciardullo, R. 1990, ApJ, 365, 471
Jedrzejewski, R. I. 1987, MNRAS, 226, 747
King, I. R., et al. 1991, AJ, 102, 1553
Krist, J. 1992, Tiny Tim Users' Manual (Baltimore: STScI)
———. 1994, Second Ann. Conf. on Astronomical Data Analysis Software and Systems (NASA: Washington)
Lauer, T. R. 1989, PASP, 101, 445
Lindsay, E. M. 1961, AJ, 6, 127
Lindsay, E. M., & Mullan, D. J. 1963, Irish Astron. J., 6, 51
Lucy, L. B. 1974, AJ, 79, 745
MacKenty, J. W., & Baggett, S. M. 1992, WFPC1 Instrument Science Report, 92-10 (Baltimore: STScI)
MacKenty, J. W., et al. 1992, Hubble Space Telescope Wide Field Planetary Camera Instrument Handbook, Version 3.0 (Baltimore: STScI)
McCarthy, J. K., Mould, J. R., Mendez, R. H., Kudritzki, R. P., Husfeld, D., Herrero, A., & Groth, H. G. 1990, ApJ, 351, 230
Meatheringham, S. J., Dopita, M. A., Ford, H. C., & Webster, B. L. 1988, ApJ, 327, 651
Meatheringham, S. J., Dopita, M. A., & Morgan, D. H. 1988, ApJ, 329, 166
Richardson, W. H. 1972, J. Opt. Soc. Am., 62, 55
Sanduleak, N., MacConnell, D. J., & Philip, A. G. D. 1978, PASP, 90, 621
Schönberner, D. 1983, ApJ, 272, 708
Snyder, D. L. 1990, in The Restoration of HST Images and Spectra, ed. R. L. White & R. J. Allen (Baltimore: STScI), 56
Vassiliadis, E., et al. 1996, ApJ, in press (Paper II)
Vassiliadis, E., & Wood, P. R. 1993, ApJ, 413, 641
Westerlund, B. E., & Smith, L. F. 1964, MNRAS, 127, 449
White, R. L. 1993, Newsletter of STSc's Image Restoration Project, 1, 11
Wood, P. R., Bessell, M. S., & Dopita, M. A. 1986, ApJ, 311, 632
Wood, P. R., Meatheringham, S. J., Dopita, M. A., & Morgan, D. H. 1987, ApJ, 320, 178
Wood, P. R., & Vassiliadis, E. 1993, in IAU Symp. 155, Planetary Nebulae, ed. R. Weinberger & A. Acker (Dordrecht: Kluwer), 465